



A micromechanical constitutive modeling of WC hardmetals using finite-element and uniform field models



Dmitry Tkalich^a, Georges Cailletaud^b, Vladislav A. Yastrebov^{b,*}, Alexandre Kane^c

^aNorwegian University of Science and Technology (NTNU), Sem Sælands veg 1, Trondheim NO-7491, Norway

^bMINES ParisTech, PSL Research University, Centre des Matériaux, CNRS UMR 7633, BP 87, Évry cedex 91003, France

^cSINTEF Materials and Chemistry, Materials and Nanotechnology, Richard Birkelandsvei 2, Trondheim NO-7465, Norway

ARTICLE INFO

Article history:

Received 26 April 2016

Revised 24 October 2016

Available online 24 November 2016

Keywords:

Cemented tungsten carbide

Microstructure

Finite element analysis

Homogenization

Uniform field model

Kröner model

Thermal residual stresses

Yield surface

ABSTRACT

For constitutive modeling of WC hardmetals we used a full field finite element simulations of accurately reproduced scanning electron microscope images and a simple uniform field two-phase model. Both models combine isotropic Drucker–Prager elastic–plastic behavior of WC grains and isotropic von Mises elastic–plastic behavior of the binder, and include non-linear hardening. We performed simulations for representative volume elements using the generalized 2.5D formulation and demonstrated a good agreement between the two models in terms of the effective mechanical behavior. Effective elastic properties and coefficients of thermal expansion were obtained. Effective yield stresses evaluated at 0.1% of effective plastic strain were also computed for six different loading paths. Probability and joint probability histograms obtained in FE simulations are presented. We also studied the effect of residual thermal stresses, which appear in WC hardmetals due to cooling from sintering temperatures. Finally, we obtained a realistic yield surface for a three-dimensional microstructure using a uniform field model with spherical inclusions. This surface combines a Drucker–Prager region for moderate pressures and a von Mises region for high pressures, with a sharp transition between these two regions. Four different WC hardmetal grades were considered. In total, nine microstructures were reproduced in finite element models with the binder content ranging from 10% to 19%. A sensitivity study on the binder plastic properties was carried out, thus the obtained results for the yield surface are applicable to real hardmetals with different binder materials and various binder content.

© 2016 Elsevier Ltd. All rights reserved.

1. Introduction

Cemented tungsten carbides are hard and tough tool-materials widely used for wear applications and metal machining. Cemented carbides consist of micro- or nano-sized tungsten carbide (WC) grains embedded in a metal matrix (binder). The term “hardmetal” is used in the current study to refer to this composite.

Over the past several decades the number of applications of hardmetals increased so considerably that it became the most prevalent tool-material today. Approximately 70% of metal cutting tools are made from hardmetals, 20% of high-speed steels, and 10% of titanium carbide-based cermets and other advanced ceramic materials (Fang and Koopman, 2014).

Hardmetals are widely employed for exploitation drilling on oil and gas, geotechnical works, or mining and different construction works, such as tunneling, road, trenching, soil stabilization, and

others. Two major fields of application of hardmetals in mining and construction can be distinguished: (1) drilling holes and wells using drilling bits and (2) cutting rock, asphalt and concrete using picks. More details about application conditions for mining and construction could be found in Kolaska (1992), Panov et al. (2004).

For hardmetals, the metallic binder content is from 3 to 30 wt% and the WC grain size ranges between 0.01 and 20 μm . They are fabricated from carbide and metal powders and the production process includes liquid and solid phase sintering at temperatures up to 1400 °C. An optimal hardness–toughness combination required for highly loaded and wear applications is achieved by combining a binder material and WC grain size, as well as by adjusting the sintering parameters.

For drilling in hard rocks (igneous rocks, e.g., basalts gabbros, granite, granodiorites and diorites) percussive drilling is employed and performed by creating high-impact loads on the rock surface. Typical percussive drilling bits with hardmetal inserts are shown in Fig. 1. Drill-bit strikes the rock at a frequency of about 2000–3000 hits per minute and rotates at about 50–150 rpm. In

* Corresponding author.

E-mail address: vladislav.yastrebov@mines-paristech.fr (V.A. Yastrebov).

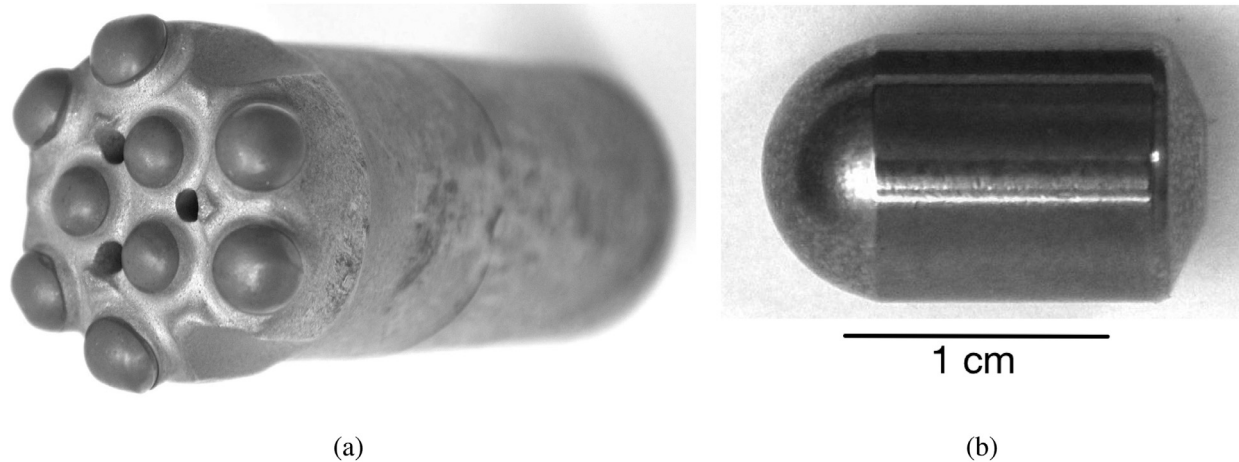


Fig. 1. Drill-bit used for percussive drilling in hard rock, equipped with 9 WC hardmetal inserts (a); single unworn drill-bit insert (b).

percussive drilling of hard rocks, gradual wear of drill-bit hardmetal inserts leads to the loss of functional shape which decreases drilling efficiency. Two modes in microstructure behavior investigation could be distinguished when developing a numerical tool for hardmetal wear assessment: in-bulk and near-surface behaviors. The current paper focuses on the construction of an elastoplastic material model for moderate homogeneous loading conditions inherent for the material in the bulk of the drill-bit insert. High normal and shear concentrated forces acting on the rock-insert contact surface and damage development should be considered in the investigation of the degradation of the material within the insert's near-surface layer. In such study the particularities of the rough rock-insert contact should be taken into account and a criterion for material deterioration (abrasive wear) could be established. SEM observation of drill-bit buttons after drilling show that severely deformed and damaged zone extends to the depth of about $10\ \mu\text{m}$ (Beste et al., 2001; Olovsjö et al., 2013). Different micro-mechanism of material deterioration are well described in the literature (Mingard and Gee, 2007; Beste and Jacobson, 2008a; Beste et al., 2008; Beste and Jacobson, 2008b; Olovsjö et al., 2013).

Two homogenization methods are utilized in the current study: (i) direct two-dimensional finite-element simulation of mechanical behavior of representative volume elements (RVE) (Kanit et al., 2003; Besson et al., 2009; Lemaitre and Desmorat, 2005) and (ii) a uniform field two-phase model, based on Eshelby's solution of the inclusion problem, extended to elasto-plasticity (Kröner, 1961; Budiansky and Wu, 1961). Utilizing the RVE concept within the finite-element (FE) simulation framework allows to obtain representative macroscopical effective behavior and also to access the local fields for arbitrary morphology and material behaviors, whereas the uniform field (UF) model is constructed using an elementary inclusion geometry (cylinder or sphere) and while predicting macroscopic effective behavior does not allow to access local fields. It is demonstrated that uniform field model predictions are in good agreement with the finite-element 2D simulation results for all studied binder content. Then the uniform field model is used to obtain effective elastic moduli and yield surface for three-dimensional case for different binder content. The results presented in this paper illustrate the behavior and stress-strain distributions in WC hardmetal for small plastic strains. Larger strains would induce plastic accommodation between the phases which is not taken into account, then damage and fracture. The approach is deliberately limited to a very simple model, in order to have in hand a non-linear constitutive equation that is simple enough to be efficient in FE calculations of real components. Constitutive behaviors for individual phases of

the hardmetal components are based on the data from the literature.

In this study we aim (i) to investigate the mechanical behavior of heterogeneous WC hardmetals and derive their effective properties from the knowledge of the constitutive laws and spatial distribution of the components, (ii) to study the statistics of stress and plastic deformation at micro-scale level and (iii) to compare results of finite-element and uniform field models at the macro-scale level.

The paper is organized as follows. Material behavior of each phase and material models are presented in Section 2. Finite-element microstructure-based models are presented in Section 3, which also includes morphological description of the microstructure, numerical aspects of the simulation and boundary conditions. Uniform field model constitutive equations are presented in Section 4. The results of FE and UF simulations are presented and discussed in Section 5. Conclusions are given in Section 6.

2. Materials

In the current section the behavior of hardmetal's constituent materials are discussed and the constitutive equations used for each phase in FE simulations are presented, together with the material parameters that are taken from other studies. Due to the absence of mechanical tests on individual phases, some uncertainties are inevitable in the model; a brief sensitivity analysis is performed in Section 5.8 in order to estimate this effect.

Hardmetals are produced by means of liquid and solid phase sintering, starting from a temperature of around $1400\ \text{°C}$, where the binder phase is in liquid state. Mechanical properties of the resultant composite are strongly affected by the sintering procedure. There are many investigations concerning the tungsten-carbon-cobalt (W-C-Co) system as cobalt is frequently used as the binder for hardmetals. A comprehensive review on the phase diagrams in W-C-binder systems can be found in Fernandes and Senos (2011). The cobalt, since it wets WC readily, exhibits a temperature-dependent solubility, which makes sintering easier and leads to products with excellent strength and ductility. Classic metallography, X-ray diffraction analysis and thermodynamical analysis are used to obtain an equilibrium at phase boundaries and isothermal sections of W-C-Co phase diagram (Rautala and Norton, 1952; Pollock and Stadelmaier, 1970). Experiments show that WC is in stable equilibrium with liquid cobalt only within a rather narrow region of compositions.

2.1. Hardmetal

Within WC hardmetal composites, the binder ensures a certain ductility whereas the tungsten carbide is responsible for high hardness and wear-resistant properties. Interfaces between the phases also play a significant role in determining overall hardmetal behavior and properties, especially at the extreme conditions near the work surface. In terms of fracture toughness, cemented WC is in general assumed to be a brittle material, and the primary failure mode for most tool applications involves chipping or fracturing.

Cemented WC hardmetals in compression may reach 1–3% inelastic deformation, originating mainly from the plastic deformation of the ductile binder and the formation of stacking faults in WC grains (Roebuck and Almond, 1988). Under bending and tensile loads close-to-linear stress–strain dependence up to failure is observed, which occurs usually at strains of 0.1–0.5% (Exner and Gurland, 1970; Jaensson, 1971; Nishimatsu, 1960).

Considerable residual thermal stresses in hardmetal composites is another important aspect in behavior of hardmetals, which was recognized in many studies (e.g. Felgar and Lubahn, 1957; Exner and Gurland, 1970; Drake and Krawitz, 1981; Chermant and Osterstock, 1976; Ingelstrom and Nordberg, 1974; Lueth, 1972; Murray, 1977; Pickens and Gurland, 1978). These residual stresses appear in the composite upon cooling from sintering temperatures to the room temperature due to the difference in thermal expansion of WC and binder phases (Exner, 1979; Spiegler and Fischmeister, 1992). Thermal residual stresses (TRS) are high and omnipresent in hardmetals (Krawitz and Drake, 2014). The mean residual stresses can be measured by several techniques (Krawitz, 2001; Reimers et al., 2008; Kisi et al., 2008; Hutchings et al., 2005), but the local specificities and the stress ranges can only be obtained by means of numerical simulations with realistic physical models for solidification taking into account metallurgical and mechanical aspects. The effect of the TRS in WC hardmetal's performance is not yet fully understood, but it is of great interest since their level is high (Krawitz and Drake, 2014). This issue will be discussed in Section 5.7. Residual stresses of other origin, e.g. surface grinding (French, 1969), are also of importance, but they are concentrated in the near-surface layer of the hardmetal and will not be discussed in this paper.

Fracture mechanisms in WC hardmetals are controversial: even the determination of the predominant ones is still under debate. They strongly depend on the binder, the composite morphology, the loading type and the grain size (Shatov et al., 2014; Almond, 1983; Chermant and Osterstock, 1976; Fischmeister, 1983; Hong and Gurland, 1983; Sigl and Exner, 1987; Slazar et al., 1986). When hardmetal is formed by micron-sized WC grains, then the ductile tearing and crack bridging in binder is the primary failure mechanism. Study of crack growth in WC hardmetal shows that 90% of the energy consumed during fracture is attributed to the plastic deformation of the metallic binder phase (Sigl et al., 1984). But, to the best of our knowledge, crack propagation near the WC grain–binder interface has not been studied in detail and it remains unclear whether the crack propagates in the binder near the interface or indeed separates binder and WC grain. In the nano-grained WC hardmetal the main deformation mechanism might not be the same. Due to the nanoscale thickness of the binder film, dislocations cannot extend sufficiently and the major deformation mechanisms change into slip along WC grain–grain interfaces and other nano-specific non-dislocation deformation (Song et al., 2013; Lay and Missiaen, 2014).

2.2. Tungsten carbide

Tungsten carbide (WC) has a hexagonal (HCP) unit cell with a c/a value of 0.976, and a lattice parameter a of 2.906 Å with

Table 1
Material properties for WC and binder.

Carbide grains, WC		
Elastic constants of transversely isotropic WC		
C_{11}	720	GPa
C_{12}	254	GPa
C_{13}	150	GPa
C_{33}	972	GPa
C_{44}	328	GPa
Homogenized isotropic Young's modulus		
E_{WC}	707.7	GPa
Homogenized isotropic Poisson's ratio		
ν_{WC}	0.197	
Initial yield stress in uniaxial compression in Eq. (2)		
R_{WC_0}	4	GPa
Friction angle in Eq. (2)		
ϕ_{WC}	45°	
Dilatation angle in Eq. (4)		
ψ_{WC}	30°	
Hardening constants in Eq. (3)		
Q_{WC}	3	GPa
b_{WC}	10	
Homogenized coefficient of thermal expansion		
α_{WC}	5.2 · 10 ⁻⁶	K ⁻¹
Binder, Cobalt		
Young's modulus		
E_B	208	GPa
Poisson's ratio		
ν_B	0.3	
Initial yield stress in Eq. (6)		
R_{B_0}	560	MPa
Hardening constants in Eq. (6)		
Q_B	607	MPa
b_B	140	
Coefficient of thermal expansion		
α_B	13.0 · 10 ⁻⁶	K ⁻¹

tungsten and carbon atoms lying at (0, 0, 0) and at (1/3, 2/3, 1/2) positions, respectively. Consequently, WC crystals exhibit a transversely isotropic elastic behavior (French, 1969; Exner, 1979; Lee and Gilmore, 1982) defined by five elastic constants. The elasticity tensor of WC crystals in Voigt notation takes the following form in a reference-frame where c is the third axis:

$$\mathbf{C}_{\sim WC} = \begin{pmatrix} C_{11} & C_{12} & C_{13} & 0 & 0 & 0 \\ \cdot & C_{11} & C_{13} & 0 & 0 & 0 \\ \cdot & \cdot & C_{33} & 0 & 0 & 0 \\ \cdot & \cdot & \cdot & C_{44} & 0 & 0 \\ \cdot & \cdot & \cdot & \cdot & C_{44} & 0 \\ \cdot & \cdot & \cdot & \cdot & \cdot & (C_{11} - C_{12})/2 \end{pmatrix} \quad (1)$$

where '·' stands for symmetrical components. The components of this tensor measured in Lee and Gilmore (1982) and refined in Golovchan and Litoshenko (2010) are listed in Table 1. In order to obtain an isotropic elastic constants for tungsten carbide, we constructed a model consisting of 2000 randomly oriented grains and used in a self-consistent homogenization framework with transversely isotropic elastic response of the grains, assuming a perfect disorder in the material Kröner (1977). The isotropic values obtained by this approach are $E_{WC} = 707.7$ GPa and $\nu_{WC} = 0.197$, they are used in the following study, in which WC grains are assumed to be isotropic.

Even though the hexagonal WC is generally considered to behave as a brittle material, slip markings are observed in WC grains in deformed hardmetals (Takahashi and Freise, 1965; Hibbs and Sinclair, 1981; Sarin and Johannesson, 1975). A significant difference of WC material strength in compression and in tension leads to the choice of a pressure-dependent yield criterion. In the present study, a Drucker–Prager yield surface is defined as follows:

$$f_{WC}(\boldsymbol{\sigma}, p) = \frac{J_2(\boldsymbol{\sigma}) + I_1(\boldsymbol{\sigma}) \tan(\phi_{WC})/3}{1 - \tan(\phi_{WC})/3} - R_{WC_0} - Y_{WC}(p), \quad (2)$$

where $J_2(\boldsymbol{\sigma}) = \sqrt{\frac{3}{2} \mathbf{s} : \mathbf{s}}$ is the von Mises stress, \mathbf{s} is the deviatoric part of the stress tensor $\boldsymbol{\sigma}$, $I_1(\boldsymbol{\sigma}) = \text{tr}(\boldsymbol{\sigma})$ is the trace of the stress tensor, then the hydrostatic pressure is given by $P = -\frac{1}{3} I_1(\boldsymbol{\sigma})$ and R_{WC_0} is the initial yield stress for a compression loading and ϕ_{WC} is the friction angle. A time independent framework is used, with an isotropic hardening defined as a function of the accumulated plastic strain p :

$$Y_{WC}(p) = Q_{WC}[1 - \exp(-b_{WC}p)], \quad \text{with}$$

$$p = \int_0^t \sqrt{\frac{2}{3} \dot{\boldsymbol{\epsilon}}^p : \dot{\boldsymbol{\epsilon}}^p} dt \quad (3)$$

where the plastic strain $\boldsymbol{\epsilon}^p$ is defined from the total and elastic strain tensors $\boldsymbol{\epsilon}^{\text{tot}}$ and $\boldsymbol{\epsilon}^e$ by $\boldsymbol{\epsilon}^p = \boldsymbol{\epsilon}^{\text{tot}} - \boldsymbol{\epsilon}^e$, and $\dot{\boldsymbol{\epsilon}}^p$ denotes its rate. A non-associated flow rule is introduced, the flow potential having the following form:

$$g_{\text{WC}}(\boldsymbol{\sigma}) = J_2(\boldsymbol{\sigma}) + \frac{1}{3} I_1(\boldsymbol{\sigma}) \tan(\psi_{\text{WC}}) \quad (4)$$

where ψ_{WC} is the dilation angle, which is set to 30°. The plastic strain tensor is then calculated, introducing the plastic multiplier $\dot{\lambda}$ to express the constraint, as follows:

$$\dot{\boldsymbol{\epsilon}}^p = \dot{\lambda} \frac{\partial g_{\text{WC}}}{\partial \boldsymbol{\sigma}} \quad (5)$$

The choice of material parameter values for the plastic behavior is based on information from the literature which shows a considerable scatter, attributed to difference in grain size and orientation (Schedler, 1988; Shatov et al., 2014; Prakash, 2014). Initial yield stress in tension and compression is chosen as an average of those reported in the literature for grain sizes between 5 and 2 μm : 2.0 GPa and 4.0 GPa, respectively. Hardening constants Q_{WC} and b_{WC} are chosen to be 3.0 GPa and 10.0, respectively. The post-yield behavior of WC grains in tension must significantly differ from that in compression, nevertheless, respecting this point is not crucial for determining the initial yield surface. Also, large plastic deformation is not expected to occur within WC grains, far from the outer work surface, where high irreversible deformation and fracture can arise due to stress concentrations originating from the contact with local rock roughness. A significant difference in plastic behavior was found for the basal and prismatic planes, as shown in an experimental study by Csanádi et al. (2014), where uniaxial compression tests on WC micropillars were performed. Such difference in work-hardening behavior (significantly higher hardening capacity observed for basal planes in comparison to the prismatic direction) can be attributed to the different slip mechanisms.

The coefficients of thermal expansion for WC crystals behavior along basal and prismatic planes (Krawitz et al., 1989) at room temperature are given in Table 1, as well as the average isotropic value used in simulations of thermal contraction.

2.3. Binder

Pools of binder material (black zones in Fig. 2) have complex shapes making a foam-like network through the bulk of WC hardmetal. The observations demonstrate that the same crystallographic structure of the binder extends on long distances within the WC hardmetal's bulk. Apparently independent on a two-dimensional section, zones of binder are most likely interconnected. These regions with the same crystallographic structure are sometimes regarded as binder "grains" (Weidow and Andrén, 2010). The linear dimension of such "grains" is typically two orders of magnitude greater than the linear dimension of WC grains (Sarin and Johannesson, 1975; Weidow et al., 2009; Mingard et al., 2011). Regardless the big dimension of similarly oriented binder channels, the local geometry of these channels form thin connections confined between carbide grains. The width of binder channels between WC grains vary and strengthening of the binder material results from the Hall–Petch-like effect (Hall, 1951; Petch, 1953), due to the reduced number of possibly active slip systems and the small mean free paths in certain direction. For an estimated average of 0.15 μm binder channel width the initial yield stress and work-hardening parameters are estimated using the Lee–Gurland model (Gurland, 1979; Lee and Gurland, 1978):

$R_{B_0} = 561$ MPa and $Q_B = 607$ MPa. The material parameters are listed in Table 1.

The binder phase is often cobalt-based but can also be iron (usually for woodworking applications), nickel (usually for applications requiring acidic corrosion resistance) or iron–cobalt–nickel alloys with a different amount of each constituent (see, e.g., Prakash, 1979; Sailer et al., 2001). The plastic binder in the composite attenuates the brittleness of the hardmetal and increases toughness. In operation, the plastic deformation in cobalt binder may reach 5–30%, depending on the synthesis method (Belteridge, 1982; Morral and Safranek, 1974), and can even rise up to 50% for nickel binder.

In the current study, it is assumed that an isotropic elasto-plastic model with a von Mises criterion and isotropic hardening can properly describe the behavior of the binder. The yield surface is defined as:

$$f_B(\boldsymbol{\sigma}, p) = J_2(\boldsymbol{\sigma}) - R_{B_0} - Y_B(p), \quad \text{with} \\ Y_B(p) = Q_B[1 - \exp(-b_B p)]. \quad (6)$$

Note that in the current study the same binder behavior and material parameters are used for all considered hardmetals regardless the actual chemical composition of certain grade binder (see Table 2). Nevertheless, for all binder types, the binder is softer and more ductile than WC grains, so that in general the behavior of the composite is well described qualitatively. Hence, here we focus more on the effect of the binder–grain morphology and on qualitatively different elasto-plastic mechanical behavior, rather than on the effect of a particular choice for the binder material.

The value of the coefficient of thermal expansion is $\alpha_B = 13 \cdot 10^{-6} \text{K}^{-1}$ (Belteridge, 1982), which is significantly higher than that for the WC. This difference results in high thermal residual stresses arising in the composite due to cooling from high sintering temperature.

2.4. Interfaces

Two types of interfaces are distinguished within the WC hardmetal microstructure: (1) WC grain–Binder, (2) WC grain–WC grain. Wetting of WC grains by liquid metallic binder determines the strength of the inter-phase interface and the cohesion of the resulting hardmetal. It was experimentally found that wetting of WC grains by molten metal is almost complete, just for some binders higher accuracy is needed to control the carbon content in the solution to avoid the formation of complex carbides (Ramqvist, 1965; Almond and Roebuck, 1988; Gille et al., 2000; Pastor, 1999). Here, WC grain–binder interfaces are not treated in any special way. It is assumed that binder material is responsible for the strength of this type of interface.

Second type of interface is the WC grain–WC grain interface. Its superior strength is achieved when the low-energy contact is formed between neighboring grains during the sintering, which was found for specific misorientations (Song et al., 2013). Atom probe field ion microscopy analysis through WC–WC interfaces showed that they contain approximately half a monolayer of Co, strictly localized to the boundary plane, and the same result was obtained using analytical electron microscopy (Henjered et al., 1986; Andrén, 2001). In this study, it is assumed that WC grain–WC grain interfaces are perfect, i.e. are not weakened by defects or impurities.

3. Finite-element model

3.1. Effective properties

The effective (average) mechanical properties of random composites may be estimated using numerous models, which estab-

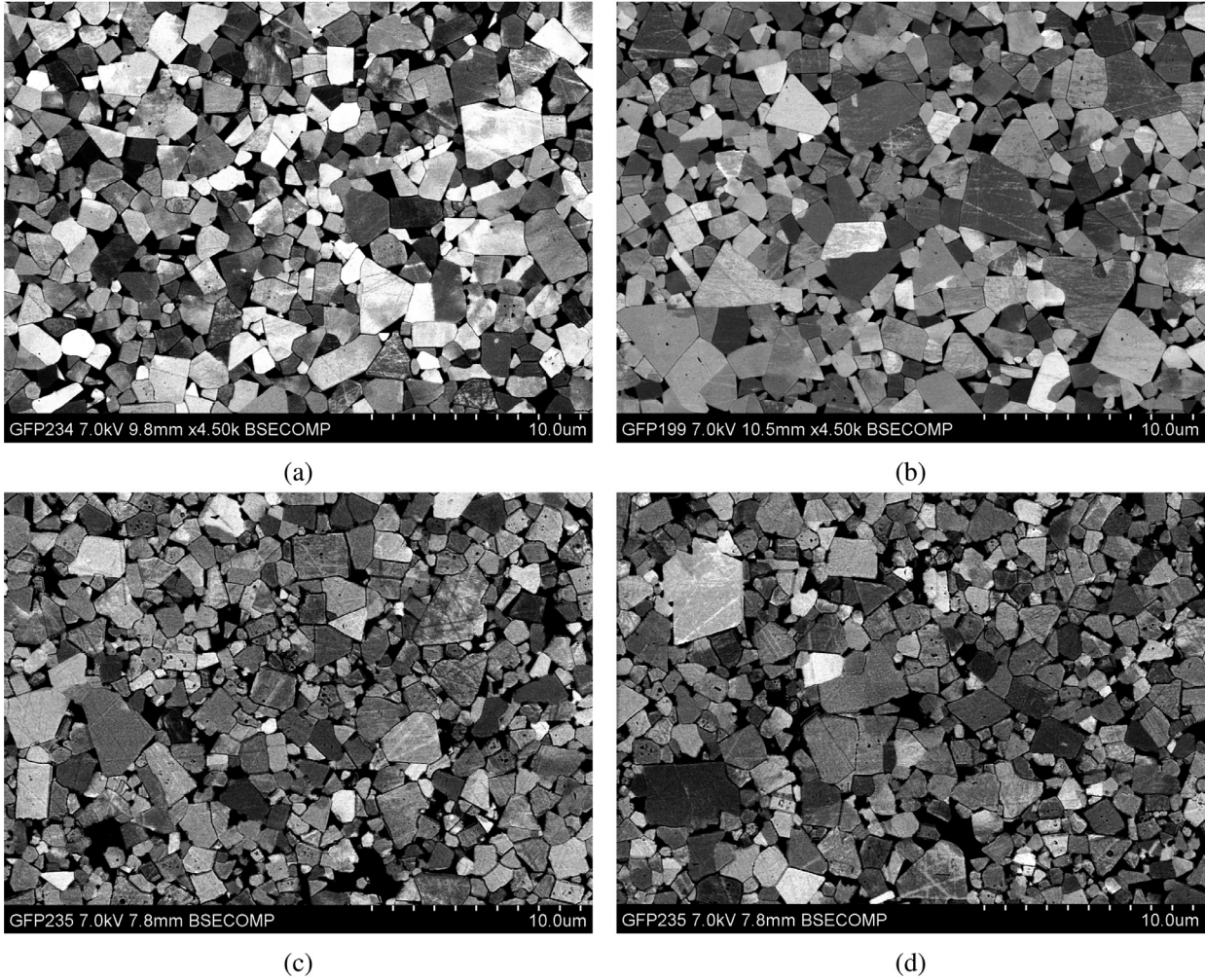


Fig. 2. SEM images of four different materials considered in this work and listed in Table 2: H1 (a), H2 (b), H3 (c), H4 (d). Light grey faceted zones correspond to WC grains and black zones correspond to the metallic binder.

Table 2
Characteristics of investigated hardmetal grades.

Name	Binder ¹ (vol%)	Binder ^a (wt%)	Binder composition ^a (wt%)	WC grain sizes characteristic ^a [μm]	Overall material density ^b [g/cm ³]
H1	9.71	6.0	Co 100%	D10=2.67, D50=3.70, D90=5.22	14.98
H2	9.71	6.0	Co 100%	D10=1.56, D50=3.52, D90=6.58	14.97
H3	9.86	6.0	Ni 85%, Fe 15%	D10=1.56, D50=3.52, D90=6.58	15.00
H4	9.53	5.7	Ni 39.4%, Fe 39.4%, Co 19.7%, Mo 1.5%	D10=1.56, D50=3.52, D90=6.58	14.92

^a Phase information prior sintering.

^b Of sintered WC hardmetal.

lish lower and upper bounds on elastic constants of the composite. The most widely-used ones for two-phase composites are: (a) Voigt and Reuss bounds, which take into account only the volume fraction of the constituent phases (Voigt, 2014; Reuss, 1929); and (b) Hashin–Shtrikman bounds which incorporate also the notion of an anisotropy of the phase distribution (Hashin and Shtrikman, 1962). Voigt's direct model and Reuss' inverse model rules of mixtures provide respectively the upper- (\bar{P}_+) and the lower-bound (\bar{P}_-) for macroscopic properties \bar{P} of a composite material as follows:

$$\bar{P}_+ = \sum_i f_{V_i} \cdot P_i \quad ; \quad \bar{P}_- = \left(\sum_i \frac{f_{V_i}}{P_i} \right)^{-1} \quad (7)$$

where P_i and f_{V_i} are the property of the interest (bulk and shear moduli) and the volume fraction of each phase, respectively. The linear mixture rule is based on the assumption of a uniform strain in the whole body, that often fails in composite materials and provides only a crude estimation of the macroscopic properties (Werner et al., 1994). Hashin–Shtrikman's bounds are obtained for a two-phase composite by assuming local and global isotropy, and the weak material embedded in the hard one or the inverse situation to get lower or upper bounds.

The self-consistent method (Hill, 1965b; Berryman, 1980; Kröner, 1981; Jeulin and Ostoja-Starzewski, 2001) proposes an estimation of the behavior that exactly corresponds to a perfect disorder in the material, that is a microstructure without any specific spatial correlation for the phases. Other theories are available, like

differential effective medium approach (Berryman, 1992; Mavko et al., 1998) and non-linear generalization of Hashin–Shtrikman bonds (Sadowski, 2005). All approaches are summarized in Besson et al. (2009), Nemat-Nasser et al. (1993).

The effective physical properties may also be estimated by means of direct numerical simulations with explicit microstructure geometries (Cailletaud et al., 2003). The approach is based on the concept of representative volume element (RVE), whose effective behavior tends to the behavior of an infinite sample as the RVE size increases (see Kanit et al., 2003; Besson et al., 2009). The accuracy of the model depends on the type of composite (regular, periodic, random), on boundary conditions (periodic, static or kinematic), on the number of realizations and on the size of the simulated domain. Both elastic and nonlinear macroscopic properties could be obtained with this approach often providing satisfactory results (Jaensson and Sundström, 1972; Chawla et al., 2002; Xu and Ågren, 2004).

Homogenization method, based on a direct simulation of the mechanical behavior of an RVE, allows to incorporate many geometrical and mechanical features in the model (Kanit et al., 2003; Besson et al., 2009; Lemaitre and Desmorat, 2005): such as material nonlinearities, complex interfaces and also possible local cracking or growth and coalescence of ductile pores (Koplik and Needleman, 1988; Tvergaard, 1990; Benzerga et al., 1999). The RVE is a geometrical model of a heterogeneous material, which is constructed based on a representative sample of its structure. The choice of its size is bound by two conditions: (i) it must be large enough to include a sufficient number of heterogeneities to be statistically representative and (ii) it must be small enough to keep the associated numerical simulation feasible. The constructed RVE finite-element model is subjected to boundary conditions to compute an effective (averaged) response of the model and also to extract relevant information on the local deformed state of individual components, which enables to perform accurate statistical analyses (Kanit et al., 2003; El Houdaigui et al., 2007). A detailed description of the method and related discussions can be found in (Besson et al., 2009; Sanchez-Palencia and Zaoui, 1987; Nemat-Nasser et al., 1993; Suquet, 1997; Castañeda, 1991; Bornert et al., 2001a; 2001b; Jeulin and Ostoja-Starzewski, 2001).

3.2. Representative volume element

Creating an RVE model for WC hardmetal microstructure is technically challenging. Simple material analysis techniques do not allow to obtain volumetric structures and the related studies are often limited to the analysis of material sections. Regardless the existence of transition rules from two to three-dimensional characteristics (Jeulin, 2013), obtaining three-dimensional models from two-dimensional experimental data presents considerable difficulties. Numerous techniques exist for creation of artificial volumetric models of material microstructures. The most widely employed introduce a Voronoi tessellation (Rycroft, 2008; Quey et al., 2011; Barbe et al., 2001a; 2001b) and the creation of polygons based on the Poisson point process (Kingman, 1992). These techniques are well-suited for microstructures of metals which possess single-type interfaces structures. As was discussed above, WC hardmetal is a composite with two types of interfaces at micro-level: “WC grain–WC grain” and “WC grain–Binder”. Reproducing such a structure is a challenge in both two- and three-dimensional spaces. A Random Sequential Addition technique (Tarjus et al., 1991) could be a possible solution for generation of a suitable bi-phase structure, but this technique does not enable to ensure realistically low binder fractions.

Four different WC hardmetal grades are used in this study. Their characteristics are listed in Table 2. WC grain size distribution in Table 2 is given in terms of x -axis values on the size distribu-

tion plot, where D10% gives the diameter such that only 10% of grains have a smaller diameter. Similarly for D50 and D90 characteristics. The grades differ in composition and processing, then in morphology and finally in mechanical characteristics. Grades H1 and H2 differ only in granulometry, the former has a more narrow distribution. The other grades have different binder but approximately the same granulometry as H2 grade. In order to obtain images of microstructures, WC inserts were cut, grinded and polished in several steps according to Struers’ method (Struers, 2016), then etched in Murakami solution for 15 s at 80 °C. Etching allows to make the morphology more pronounced. SEM images were taken using 20 kV accelerating voltage and 80–100 nA probe current. Examples of backscatter electron (BSE) images used for creation of finite-element (FE) models are shown in Fig. 2 for each investigated grade. Light grey faceted zones correspond to WC grains, whereas black zones identify the metallic binder.

The shape of WC grains and their interconnections are the main morphological aspects which may influence the mechanical behavior of the composite. The high volume fraction of WC (80–95%) imposes rather stiff constraints on the shape of WC grains and on the morphology of the binder. The shape of WC grains within hardmetal bulk forms from tungsten carbide powder during sintering. The final WC grain shapes, size distribution and binder phase structure depend on the sintering time, the amount of liquid binder phase, and on carbon and tungsten contents (Borgh et al., 2013; Kim et al., 2008; Lay et al., 2008; Chabretou et al., 2003; Marshall and Giraudel, 2015). When unconfined, WC grains take shape of a faceted triangular prism with truncated corners (delimited by basal and prismatic facets) (Exner, 1979), but within the sintered hardmetal, bulk WC grains are better described as faceted spheres or Voronoi polygons, as shown in a recent study on 3D shapes of WC grains (Borgh et al., 2013). During sintering, WC grains grow and their shapes get determined by the anisotropy in WC-binder interface energy (Herring, 1951).

Another important characteristic of WC hardmetal is the presence of two types of interfaces. Results of section morphological analysis presented in Table 3 show that a significant amount (in average 40%) of the grain perimeter presents interfaces between neighboring WC grains, meanwhile the rest of the grain perimeter is bounded by the binder material. Connected WC grains form a “skeleton”, whose actual connectivity is still a matter of debate (Warren and Waldron, 1972; Nelson and Milner, 1972; Gurland and Norton, 1952; Andrén, 2001; Lay and Missiaen, 2014). A thin layer of binder material, too small to be recognized in SEM images, can sometimes be found between two adjacent grains (Beste and Jacobson, 2008a; Beste et al., 2008; Beste and Jacobson, 2008b), in most cases such interfaces appear as a discontinuous monolayer of the binder material. So, WC grains form a skeleton, in which binder is present as grain boundary segregation.

3.3. Model creation

In order to obtain precise stress distributions, the geometrical models of studied hardmetals are created based on 2D SEM images shown in Fig. 2. The geometry of grains was manually outlined using the pre-processing module of Abaqus/CAE software. Similar 2D model creation approach could be found, for instance, in Sadowski and Nowicki (2008). The resulting two-dimensional sketches were used to create nine geometrical models with dimensions $19.5 \times 19.5 \mu\text{m}^2$. The representativity of the models will be assessed in Section 5.2. The procedure of model construction is then illustrated in Fig. 3. The morphological characteristics of each model are given in Table 3. It is known that the morphological characteristics at macroscopic scale (cm) may vary from the surface to the bulk within WC hardmetal inserts (Murray et al., 2005; Zhang et al., 2010). That is the case for functionally graded materials, but

Table 3
Morphological characteristics of nine geometrical models $19.5 \times 19.5 \mu\text{m}^2$ created using SEM images.

Grade name	Section ID	Number of grains	Binder (area %)	Mean WC grain section area [μm^2]	% of WC boundaries shared with other WC
H1	1	408	13.0	0.80	38.0
	2	339	12.8	0.97	40.3
	3	350	14.0	0.93	37.7
H2	1	380	11.4	0.88	41.5
	2	366	10.0	0.93	45.5
H3	1	421	19.0	0.73	30.8
	2	405	17.7	0.77	29.5
H4	1	492	14.0	0.66	37.0
	2	460	14.2	0.70	36.0

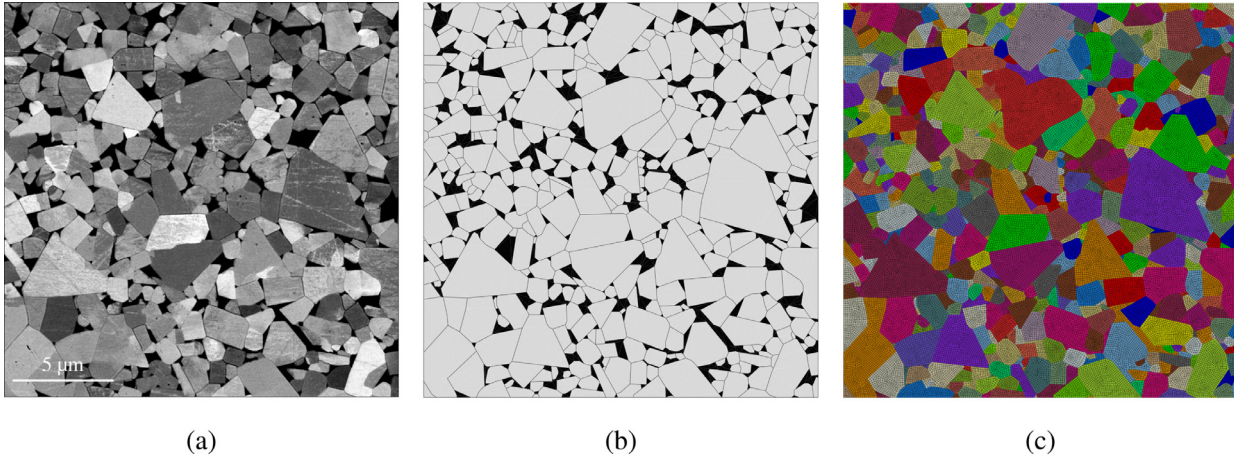


Fig. 3. Schematic illustration of the creation process of a representative volume element: (a) SEM images, (b) outlined geometry with preserved straight interface boundaries, (c) finite element mesh.

also for conventional grades, due to boundary effects. The zones far from insert's outer work surface were chosen when recording SEM images of grades' microstructures. The binder content and WC grain size distribution vary considerably from zone to zone even within a single grade. Among all recorded images, only those were chosen for RVE models, which respects the average composition.

A careful manual model creation procedure ensures preserving a correct phase fraction and the morphological structure within the chosen zone. Some problems were encountered in determining whether the zone between neighboring WC grains is a thin binder channel or a pure grain–grain boundary. It was helpful to use images of the zone obtained using both electron backscatter diffraction and secondary-electron modes.

We targeted to preserve straight boundaries of grains. Having an accurate representation of straight interfaces is critical for the accuracy of the stress field near the interface and hence is critical for the accurate simulation of plastic deformations (Barbe et al., 2001a; 2001b). Inevitable strain singularities at angles, which are inherent to the considered microstructure, lead to high concentration of plastic strain and affect the onset of plasticity both on the microscopic and macroscopic scales.

3.4. Finite-Element simulation details

In the current study, we use computational homogenization technique employing linear and non-linear FE analysis in Z-set software (Z-set, 2016; Besson and Foerch, 1997). Quasi-static simulations and small deformation formulation are used. Linear quadrilateral finite elements with selective integration are used to avoid strong variation of hydrostatic pressure inside elements.

A generalized plane strain element formulation (or 2.5D) is used for all the calculations. The constitutive equations take then

their three-dimensional expression. Six global degrees of freedom are added to the 2D mesh, in order to control the overall rotations and possible translations of the whole face. In the simulations, the rotational degrees of freedom and the in-plane translations are set to zero. Only the out-of-plane translation (z direction) remains free. This formulation allows the out-of-plane normal strain to be uniform, meanwhile the resulting force in z direction will remain equal to zero, that provides a state of plane stress for the macroscopic RVE, but allows the local variation of out-of-plane stresses.

Regarding the in-plane boundary conditions, a combination of kinematic (Dirichlet) uniform boundary conditions (KUBC) and static (Neumann) uniform boundary conditions (SUBC) are used to investigate the behavior of the hardmetal RVE. The following boundary conditions are used: (i) in all loadings normal displacements are fixed on the surface $y = 0$: $u_y = 0$ and on the surface $x = 0$: $u_x = 0$; (ii) normal displacements u_x or/and u_y are prescribed at boundaries $x = L$ and $y = L$, respectively, where L is the size of the RVE. Prescribed displacements result in effective (average) strains (E_{ij}) and trivial Neumann boundary conditions result in effective strains ($\Sigma_{jj} = 0$). When RVE boundary is free of displacement constraints (uniaxial compression or uniaxial tension cases) no traction is imposed on the free boundary but a multipoint constraint is applied keeping this side straight. Thermal expansion properties are assumed isotropic (see Table 1). Six different loadings are used:

- (1) equibiaxial compression: $E_{xx} = E_{yy} < 0$;
- (2) unsymmetric biaxial compression: $E_{xx} = 2E_{yy} < 0$;
- (3) compression along x : $E_{xx} < 0$, $\Sigma_{yy} = 0$;
- (4) pure shear strain: $E_{xx} < 0$, $E_{yy} = -E_{xx}$;
- (5) tension along x : $E_{xx} > 0$, $\Sigma_{yy} = 0$;
- (6) equibiaxial tension: $E_{xx} = E_{yy} > 0$.

4. Uniform field model

The uniform field (UF) model used to obtain effective non-linear behavior of the two-phase medium is discussed in this section. In contrast with finite-element homogenization approach, which is based on models closely resembling real composite morphology, uniform field homogenization approach simply estimates the averaged response of a given phase, seen as a single inclusion, by collecting its occurrences in the composite. As a consequence, this inclusion is surrounded by the homogeneous equivalent medium. Shape of the inclusion is chosen according to a global anisotropy of the real composite, where, for instance, spherically and cylindrically shaped inclusions are used for a macroscopically isotropic and transversely isotropic composites, respectively. Obtaining compatible and balanced stresses and strains in both the inclusion and the surrounding medium would be the solution of such inclusion problem, which was done by Eshelby (1957). Such inclusion problem is solved for each composite's phase obtaining a set of equations defining stress and strain in each phase together with the macroscopic response.

The starting point is the approach proposed by Kröner (1961) and Budiansky and Wu (1961). For a two-phase materials, with a distinct elastic behavior in each phase, the model can be summarized by:

$$\sigma_i = \Sigma + \tilde{\mathbf{C}} : (\mathbf{S}^{-1} - \mathbf{I}) : (\mathbf{E} - \boldsymbol{\varepsilon}_i), \quad (8)$$

where σ_i , $i = 1, 2$ are the uniform stress tensors in each phase, and $\boldsymbol{\varepsilon}_i$, $i = 1, 2$ are the uniform strain tensors in each phase. The tensors Σ and \mathbf{E} are respectively the average stress and strain tensors. The expression of the model derives from Eshelby's solution. The fourth order tensor $\tilde{\mathbf{S}}$ is the Eshelby tensor, that depends on the shape of the inclusion and on the properties of the homogenized medium, \mathbf{I} is the fourth-order symmetric unit tensor and $\tilde{\mathbf{C}}$ is the macroscopic elastic tensor.

This approach was extended to the elasto-plastic case, by considering the strain partition global one and in each phase, namely:

$$\mathbf{E} = \tilde{\mathbf{C}}^{-1} : \Sigma + \mathbf{E}^p + \mathbf{E}^{th}, \quad \boldsymbol{\varepsilon}_i = \tilde{\mathbf{C}}_i^{-1} : \sigma_i + \boldsymbol{\varepsilon}_i^p + \boldsymbol{\varepsilon}_i^{th}, \quad (9)$$

where \mathbf{E}^p and \mathbf{E}^{th} are the macroscopic plastic and thermal strain tensors, respectively, $\boldsymbol{\varepsilon}_i^p$ and $\boldsymbol{\varepsilon}_i^{th}$ are the uniform plastic and thermal strain tensors of phase "i", respectively, and $\tilde{\mathbf{C}}_i$ are the fourth order tensors of the elastic moduli of each phase. Substituting Eq. (9) into Eq. (8) allows to obtain the expression of the stress in each phase:

$$\sigma_i = \mathbf{A}_i : \left[\Sigma + \tilde{\mathbf{C}}^* : (\mathbf{E}^p + \mathbf{E}^{th} - \boldsymbol{\varepsilon}_i^p - \boldsymbol{\varepsilon}_i^{th}) \right], \quad (10)$$

where $\tilde{\mathbf{C}}^* = \tilde{\mathbf{C}} : (\mathbf{I} - \tilde{\mathbf{S}})$ and the fourth order tensor \mathbf{A}_i depends on the local and the macroscopic elastic tensors, and on Eshelby's tensor. It introduces a correction due to the non-uniform elasticity:

$$\mathbf{A}_i = \left[\tilde{\mathbf{C}} : \tilde{\mathbf{S}} : \tilde{\mathbf{C}}^{-1} + \tilde{\mathbf{C}}^* : \tilde{\mathbf{C}}_i^{-1} \right]^{-1}. \quad (11)$$

The main feature of the model is the correction due to the plastic and thermal strains. The corrective term for plastic strain is known to be much too big for large plastic strains (Berveiller and Zaoui, 1979). The intergranular stresses estimated by the model are then too large as well. An alternative solution is then proposed by Hill's self-consistent model (Hill, 1965a), which reformulates the equations in a rate form, and introduces tangent operators instead of elastic ones. The non-linearity of the operators ensures a plastic accommodation instead of an elastic accommodation and generates reasonable residual stress levels. A third solution has recently been proposed for the case of a uniform elasticity in various

phases (Cailletaud and Pilvin, 1994) and for non-uniform elasticity (Cailletaud and Couduon, 2016). In this case, the non linearity is introduced by means of a new accommodation variable β with a non linear evolution. The corresponding equation, expressed without thermal strain for the sake of simplicity, writes:

$$\sigma_i = \mathbf{A}_i : \left[\Sigma + \tilde{\mathbf{C}}^* : (\beta - \beta_i) \right], \quad (12)$$

The variables β_i represent the accommodation tensor in each phase, and β is the corresponding macroscopic value. The following evolution rules are introduced:

$$\dot{\beta}_i = \dot{\boldsymbol{\varepsilon}}_i^p - D \beta_i || \dot{\boldsymbol{\varepsilon}}_i^p || \quad (13)$$

The parameter D is used to control the non linearity of the stress redistribution. It should be calibrated by finite element calculations (Cailletaud and Couduon, 2016). The value of β is deduced from the β_i by using the fact that the average of the local stresses is nothing but the macroscopic stress:

$$\beta = \left\langle \mathbf{A}_i : \tilde{\mathbf{C}}^* \right\rangle^{-1} : \left\langle \mathbf{A}_i : \tilde{\mathbf{C}}^* : \beta_i \right\rangle \quad (14)$$

Since the purpose of the present paper is limited to the initial yield and very first stages of elasto-plastic deformations, the simulations will be performed with the original version of the Kröner's model. The Eshelby tensors is chosen according to the morphology of the material. For the 2D case, the inclusion is cylindrical, so that (\mathbf{S}_{cyl}) to be used is:

$$\mathbf{S}_{\text{cyl}} = \begin{pmatrix} S_{11} & S_{12} & S_{13} & 0 & 0 & 0 \\ S_{12} & S_{11} & S_{13} & 0 & 0 & 0 \\ 0 & 0 & 0 & 0 & 0 & 0 \\ 0 & 0 & 0 & 1/4 & 0 & 0 \\ 0 & 0 & 0 & 0 & 1/4 & 0 \\ 0 & 0 & 0 & 0 & 0 & S_{66} \end{pmatrix}, \quad (15)$$

where $S_{11} = (5C_{11} + C_{12})/8C_{11}$, $S_{12} = (3C_{12} - C_{11})/8C_{11}$, $S_{13} = C_{13}/2C_{11}$, $S_{66} = (3C_{11} - C_{12})/8C_{11}$, and where C_{ij} are the components of the effective elasticity tensor $\tilde{\mathbf{C}}$, the third component corresponds to the out-of-plane axis. For the 3D case, the Eshelby's tensor for the spherical inclusion (\mathbf{S}_{sph}) is used:

$$\mathbf{S}_{\text{sph}} = \frac{1}{15(1-\nu)} \left[(5\nu - 1) \mathbf{I} \otimes \mathbf{I} + 2(4 - 5\nu) \tilde{\mathbf{I}} \right], \quad (16)$$

where $\mathbf{I} \otimes \mathbf{I} \sim \delta_i^j \delta_k^l$ is the second-rank identity tensor, and $\tilde{\mathbf{I}} \sim \frac{1}{2} (\delta_i^k \delta_j^l + \delta_i^l \delta_j^k)$ is the symmetric part of the fourth-rank identity tensor. The iterative scheme for obtaining the effective elasticity tensor is as follows:

$$\tilde{\mathbf{C}}_{\sim k} = \sum_{i=WC,B} f_i \tilde{\mathbf{C}}_i : \left[\mathbf{I} + \mathbf{S}_i : \left(\tilde{\mathbf{C}}_{\sim k-1}^{-1} : \tilde{\mathbf{C}}_i - \mathbf{I} \right) \right]^{-1}, \quad (17)$$

where f_i is the volume fraction of "i"th phase, k is the iteration step number and the initial guess of the effective elasticity tensor $\tilde{\mathbf{C}}_{\sim 0}$ for our two-phase composite is:

$$\tilde{\mathbf{C}}_{\sim 0} = f_1 \tilde{\mathbf{C}}_{\sim 1} + (1 - f_1) \tilde{\mathbf{C}}_{\sim 2}. \quad (18)$$

The elasticity tensors $\tilde{\mathbf{C}}_{\sim 1}$ and $\tilde{\mathbf{C}}_{\sim 2}$ are those of the binder and the WC materials. They are isotropic and constructed using the parameters E_{WC} , ν_{WC} , E_B and ν_B from Table 1. The constitutive equations for the plastic behavior of both phases were presented in Section 2.2 and Section 2.3 with material parameters as given in Table 1.

The UF model constructed for a cylindrical inclusion Eq. (15), is compared with 2D FE simulations in Section 5. In additions, Section 5.9 shows the construction of the yield surface for 3D model with the uniform field model, using Eshelby's tensor for the spherical inclusion Eq. (16).

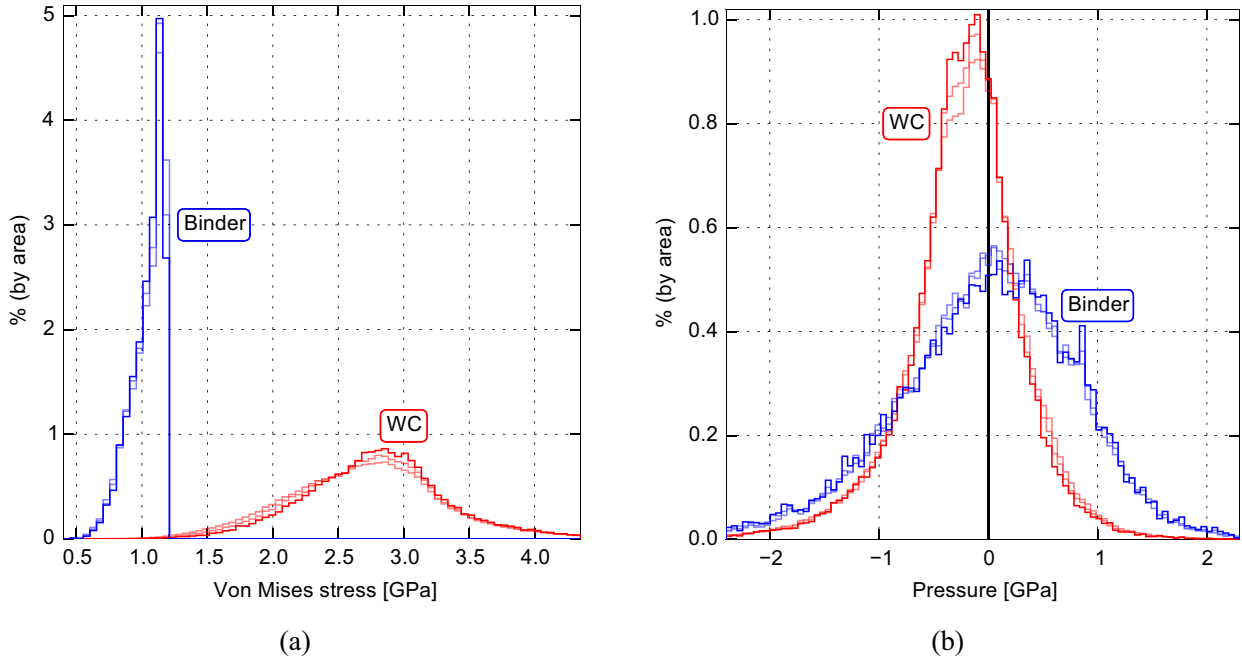


Fig. 4. Mesh sensitivity check for shear test. Histogram of von Mises stress (a) and pressure (b) are presented for three different mean element sizes: 0.1, 0.05 and 0.025 μm , stress distributions in WC and Binder phases are shown separately.

5. Results

Results presented below are those obtained with 2D FE model and UF model, constructed for a cylindrical inclusion problem. Therefore, the effective elasticity tensor is transversely isotropic and the yield surface are shown only in σ_1 - σ_2 2D principal stress space. Results obtained with UF model, constructed for a spherical inclusion problem, and thus exhibiting isotropic behavior, are presented in Section 5.9.

5.1. RVE Size and mesh sensitivity

The question of sufficiency of the size of the RVE is governed by Hill-Mandel's lemma (see e.g. (Besson et al., 2009)). A formal criterion of the sufficiency of the RVE size is based on inequality obtained in Huet (1990) demonstrating that the true effective tensor of elastic moduli $\tilde{\mathbf{C}}$ is bounded by elastic tensor obtained numerically with SUBC and KUBC boundary conditions:

$$\tilde{\mathbf{C}}^{\text{SUBC}} \leq \tilde{\mathbf{C}} \leq \tilde{\mathbf{C}}^{\text{KUBC}}$$

For the chosen RVE of $19.5 \times 19.5 \mu\text{m}^2$ the difference in Young's modulus obtained with SUBC and KUBC is smaller than 0.2%. The second criterion is that Young's modulus in x and y direction coincide with accuracy $<1\%$, which suggest that the isotropy is preserved. The third criterion is that our FEM predictions coincide with elastic moduli yielded by the UF model with accuracy of $\approx 1\%$. These three criteria ensure that the size of RVE was chosen sufficiently big to provide us with accurate results both in elastic and in the onset of elasto-plastic regimes.

Mesh sensitivity was checked by obtaining stress distributions for three different meshes with mean element sizes: 0.1, 0.05 and $0.025\mu\text{m}$. Distribution histograms of the von Mises stress and pressure for three different mesh sizes are shown in Fig. 4. The stress state corresponds to a non-linear regime in which plasticity is present in both phases, and maximal shear strain applied $\varepsilon_{xy} = 0.12\%$. No significant influence of the mesh size on the stress distribution is found. Element size of $0.1\mu\text{m}$ is used in the following simulations.

5.2. Elastic moduli

A series of FE simulations is conducted employing isotropic elasticity for WC and binder materials in order to determine the effective elasticity tensors for the considered WC hardmetal models. Material parameters for each phase are given in Table 1. Generalized plane strain element formulation is used with compressive and shear KUBC.

Compliance tensor components (S_{ij}) are determined by solving the system of linear equations given by the following relation between effective stresses Σ_{ij} and strains E_{ij} (Voigt notation is used, zero lines are omitted):

$$\begin{pmatrix} E_{xx} \\ E_{yy} \\ E_{zz} \\ E_{xy} \end{pmatrix} = \begin{pmatrix} S_{11} & S_{12} & S_{13} & 0 \\ \cdot & S_{11} & S_{23} & 0 \\ \cdot & \cdot & S_{33} & 0 \\ \cdot & \cdot & \cdot & S_{66} \end{pmatrix} \begin{pmatrix} \Sigma_{xx} \\ \Sigma_{yy} \\ \Sigma_{zz} \\ \Sigma_{xy} \end{pmatrix}, \quad (19)$$

where, for V being the total volume of the RVE model:

$$E_{ij} = \frac{1}{V} \int_V \varepsilon_{ij} dV, \quad \Sigma_{ij} = \frac{1}{V} \int_V \sigma_{ij} dV \quad (20)$$

and ε_{ij} and σ_{ij} are the components of strain and stress tensors, respectively. Effective elastic moduli determined with uniform field model (UF) using Eq. (17) and with 2D finite-element simulations (FE) using Eq. (19) are given in Table 4 for all considered RVEs. In Fig. 5(a) in-plane normalized effective Young's moduli determined from FE simulations for each model together with Hashin-Shtrikman bounds are depicted. Experimental investigations (Doi et al., 1970; Okamoto et al., 2005; Koopman et al., 2002) reported that the elastic moduli depend solely on the volume fraction of the carbide crystals for the WC-(1–30)wt% Co composites. They neither depend on the mean linear intercept of WC grains nor do they change with the carbon content (even when the binder phase is non-uniformly distributed). Result of the current numerical simulations (see Fig. 5(a)) show approximately linear dependence of the effective Young's modulus on the binder content. Experimental measurements of the Young's modulus of hardmetal, as reported, for instance, in Doi et al. (1970), Koopman et al. (2002) show also

Table 4

Effective Young's moduli and Poisson's ratios for each microstructure obtained using FE and UF models, and the relative error. Subscript "p" stands for in-plane and "z" stands for out-of-plane properties. Results are sorted by binder content.

Binder [area %]	Model	E_p [GPa]			E_z [GPa]		
		FE	UF	Δ [%]	FE	UF	Δ [%]
10.0	H2-2	618.9	622.3	0.55	657.5	658.2	0.12
11.4	H2-1	607.3	611.0	0.61	650.4	651.2	0.12
12.8	H1-2	596.3	599.9	0.60	643.8	644.3	0.08
13.0	H1-1	592.4	598.4	1.01	641.7	643.3	0.25
14.0	H1-3	586.2	590.6	0.75	637.9	638.3	0.06
14.0	H4-1	586.6	590.6	0.68	638.0	638.3	0.05
14.2	H4-2	585.2	589.0	0.65	636.8	637.3	0.08
17.7	H3-2	558.6	562.6	0.72	619.5	619.9	0.07
19.0	H3-1	547.5	553.1	1.02	612.1	613.5	0.23

Binder [area %]	Model	ν_{pp}			ν_{zp}		
		FE	UF	Δ [%]	FE	UF	Δ [%]
10.0	H2-2	0.219	0.220	0.46	0.199	0.199	0.03
11.4	H2-1	0.221	0.223	0.91	0.199	0.199	0.01
12.8	H1-2	0.225	0.226	0.45	0.199	0.199	0.01
13.0	H1-1	0.226	0.226	0.08	0.199	0.199	0.01
14.0	H1-3	0.228	0.229	0.44	0.199	0.199	0.02
14.0	H4-1	0.227	0.229	0.88	0.200	0.199	0.02
14.2	H4-2	0.227	0.229	0.88	0.200	0.200	0.02
17.7	H3-2	0.234	0.236	0.86	0.201	0.201	0.01
19.0	H3-1	0.238	0.239	0.42	0.201	0.201	0.01

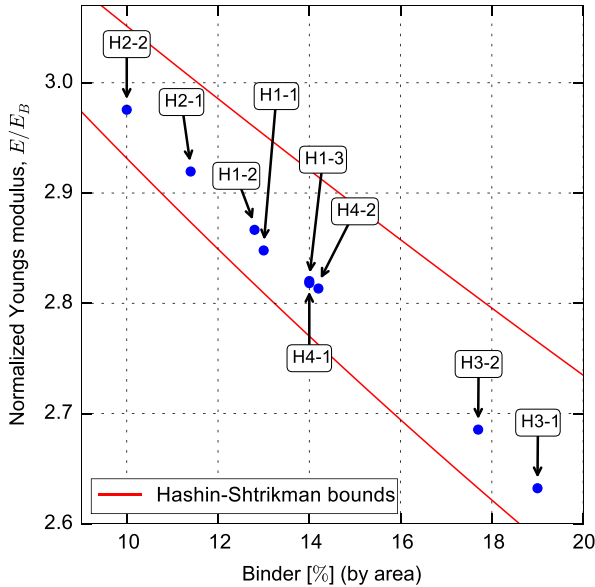


Fig. 5. In-plane effective Young's moduli for each model in case of isotropic elastic WC grains (a). All effective Young's moduli are normalized by the Young's modulus of the binder material ($E_B = 208$ GPa).

close-to-linear dependence on the binder content in the fraction's interval of the interest.

5.3. Coefficient of thermal expansion

In this section, effective coefficient of thermal expansion (CTE) α is determined for the WC hardmetal. A series of FE simulations is conducted employing isotropic elasticity and isotropic thermal deformation properties for both WC and binder materials. Material parameters are given in Table 1. Generalized plane strain element formulation is used within a thermo-mechanical formulation.

Table 5

Effective coefficients of thermal expansion for each microstructure obtained using FE and UF models, and the relative error. Subscript "p" stands for in-plane and "z" stands for out-of-plane properties. Results are sorted by binder content.

Binder [area %]	Model	$\alpha_p (-10^{-6})$ [1/K]			$\alpha_z (-10^{-6})$ [1/K]		
		FE	UF	Δ [%]	FE	UF	Δ [%]
10.0	H2-2	5.71	5.68	0.53	5.87	5.84	0.51
11.4	H2-1	5.77	5.75	0.35	6.02	5.93	1.52
12.8	H1-2	5.86	5.82	0.69	6.07	6.03	0.66
13.0	H1-1	5.87	5.83	0.69	6.12	6.04	1.33
14.0	H1-3	5.89	5.88	0.17	6.23	6.12	1.80
14.0	H4-1	5.92	5.88	0.68	6.18	6.12	0.98
14.2	H4-2	5.96	5.89	1.53	6.15	6.13	0.33
17.7	H3-2	6.13	6.08	0.82	6.45	6.38	1.10
19.0	H3-1	6.18	6.15	0.49	6.63	6.48	1.32

Thermal strains in three principal directions (E_{ii}^{th}) are determined from the following system of linear equations:

$$\begin{pmatrix} E_{xx}^{th} \\ E_{yy}^{th} \\ E_{zz}^{th} \end{pmatrix} = \begin{pmatrix} E_{xx} \\ E_{yy} \\ E_{zz} \end{pmatrix} - \begin{pmatrix} S_{11} & S_{12} & S_{13} \\ \cdot & S_{11} & S_{23} \\ \cdot & \cdot & S_{33} \end{pmatrix} \begin{pmatrix} \Sigma_{xx} \\ \Sigma_{yy} \\ \Sigma_{zz} \end{pmatrix}. \quad (21)$$

Coefficient of thermal expansion is then obtained using:

$$\alpha_i = E_{ii}^{th} / \Delta T. \quad (22)$$

where ΔT is the prescribed temperature change. Effective CTE determined for each microstructure in each direction obtained using FE and UF models are presented in Table 5. A consistent increase of both α_p and α_z with binder content is observed.

5.4. Stress-strain curves

Comparison of results of the uniform field model and effective responses of RVE from FE simulations in different loading cases are shown in Fig. 6 for equibiaxial loading, in Fig. 7 for uniaxial loadings and in Fig. 8 for shear. Within the UF model stresses and strains in both phases are calculated using Eq. (10). The plots

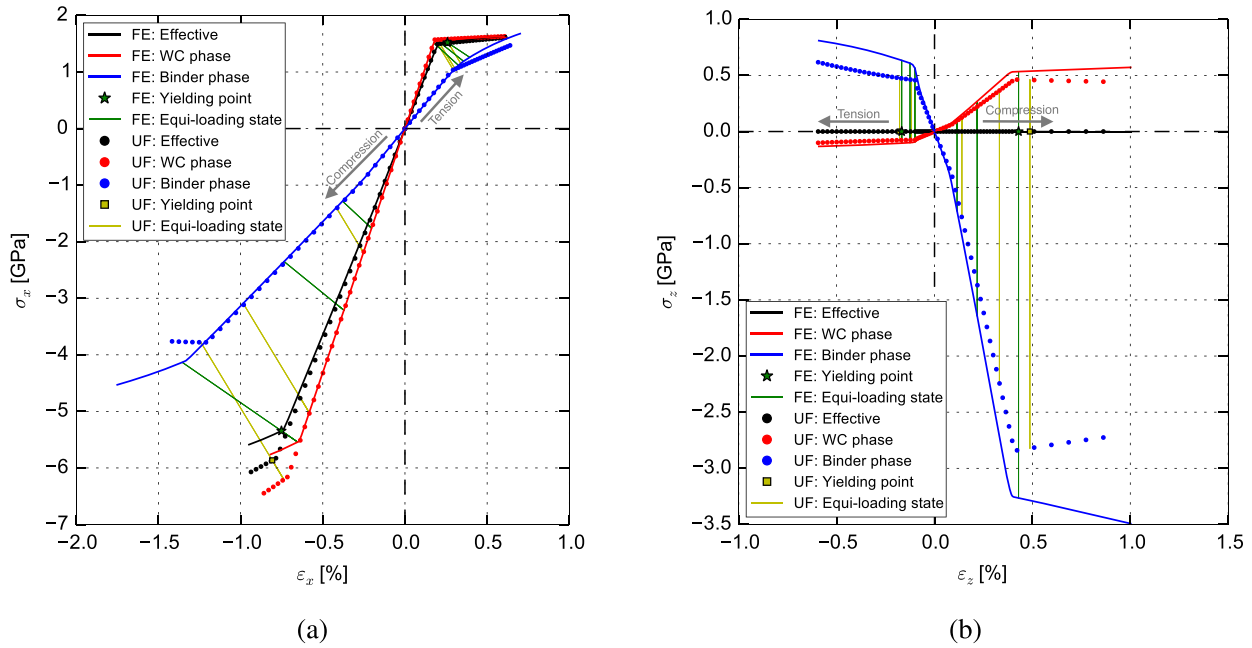


Fig. 6. Stress–strain curves for “H1-3” model under equibiaxial compression and tension obtained using FE and UF models. Deformation curves are presented in-plane “x”(a) and in out-of-plane direction “z”(b) directions.

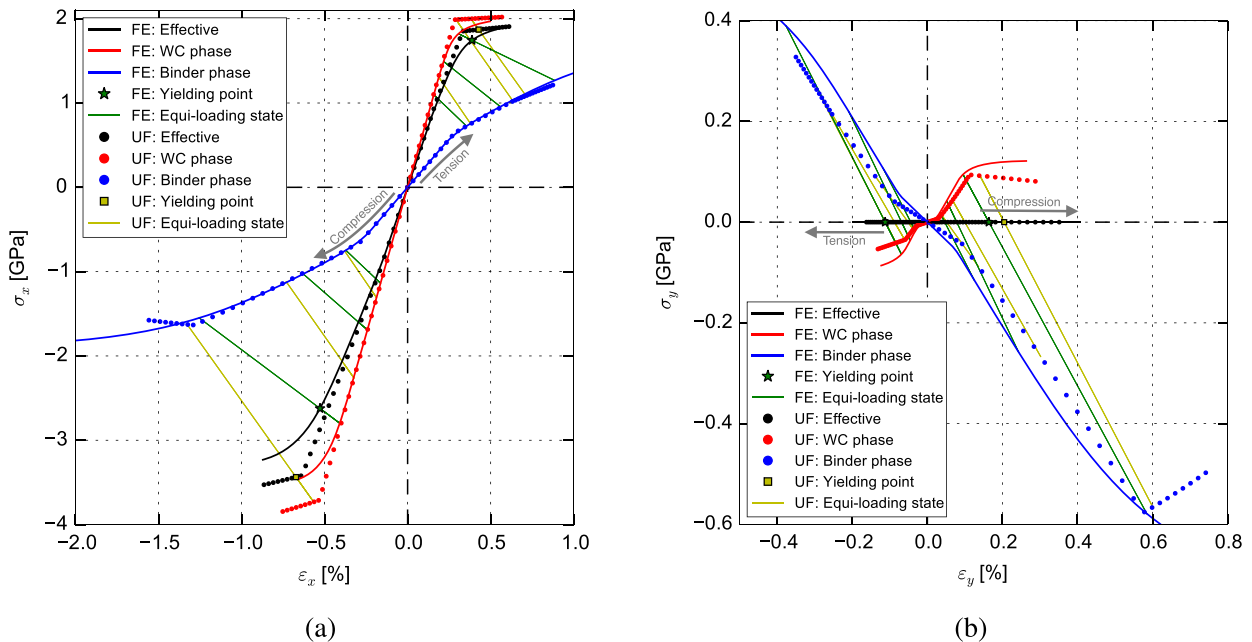


Fig. 7. Stress–strain curves for “H1-3” model under uniaxial compression and tension (loading is in “x” direction) obtained using FE and UF models. Deformation curves are presented in-plane “x”(a) and “y”(b) directions.

show the stress–strain curves obtained within each phase and at the macro-scale. Three time steps, namely those where the macroscopic plastic strain value (see Section 5.5) is 0.005%, 0.025% and 0.1%, were selected to highlight the corresponding points for the three curves. The last one is nothing but the chosen threshold for the determination of the macroscopic yield stress. In agreement with the UF model formulation, these points on three curves (total effective, WC phase average and Binder phase average) are aligned with a constant slope for the three deformation levels. They are also aligned for the case of FE. As expected, the slopes are in good agreement at the onset of plastic flow, as the elastic accommodation used in the UF model is quite accurate when plastic strains

are small. At larger strains, due to the increase of plastic accommodation, the FE solution deviates from the behavior predicted by the UF model. A model employing non-linear evolution of the accommodation tensors β_i in each phase (see Eq. (13)) would give a more accurate results in the large deformation regime.

The consequence of the “generalized plane strain” assumption is shown in Fig. 6(b), where the out-of-plane components (“z” direction) have the same values in the phases and at the macro-scale for a given time step. The agreement between FE and UF is perfect for the elastic regime, and acceptable at the onset of plastic flow. As expected, for larger plastic strains, average stresses in FE simulation are lower than those predicted by the UF model. The agree-

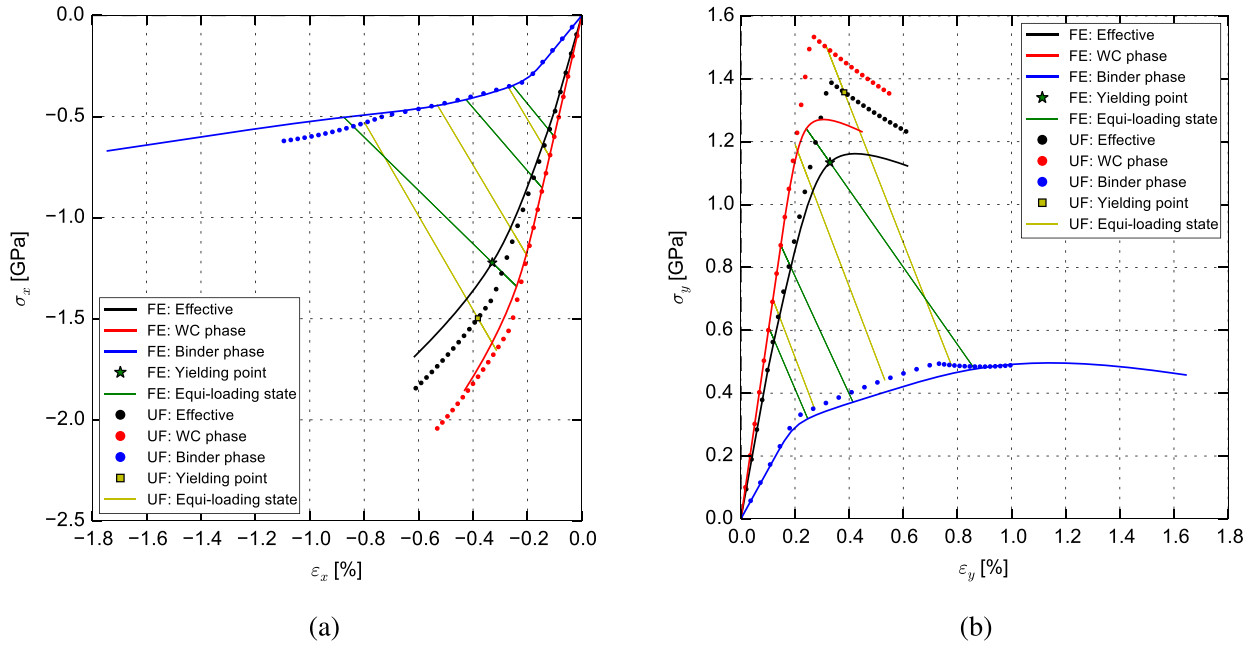


Fig. 8. Stress–strain curves for “H1-3” model under shear (compression in “x” direction) obtained using FE and UF models. Deformation curves are presented in-plane “x”(a) and “y”(b) directions.

ment is good also for uniaxial tension and compression, where the main difference between FE and UF is observed in compression for WC and the macroscopic curve. In the case of “shear” loading, as shown in Fig. 8, an asymmetry is present between “x” and “y” components. This is the result of non-preserving-volume plastic flow behavior, assigned to the volume-dominant WC phase, which results in a decrease of tensile (here $-\sigma_y$) and in an increase of compressive (here $-\sigma_x$) stresses.

It is worth mentioning that UF model is able to qualitatively capture the unloading originating from the onset of plastic flow in WC phase (Fig. 8b).

5.5. Yield stresses

Effective yield stresses are determined for each microstructure model using relations between effective stresses and strains. The yield stress for each type of loading (presented in Section 3.4) was identified as the point at which the effective equivalent plastic strain reaches 0.1%. The effective equivalent plastic strain (\bar{p}) is defined by:

$$\bar{p} = \sqrt{\frac{2}{3} \mathbf{E}^P : \mathbf{E}^P} \tag{23}$$

where \mathbf{E}^P is the effective plastic strain tensor, which is computed as follows:

$$\mathbf{E}^P = \mathbf{E} - \mathbf{C}^{-1} : \boldsymbol{\Sigma} \tag{24}$$

Yield stresses obtained using finite-element simulations and the uniform field model for the nine investigated microstructures are given in Table 6 and shown in Fig. 9 in 2D principal stress space (σ_1 – σ_2). Results show that the higher binder content results in lower yield stress in all loading cases, but the effect is much more pronounced in compression than in tension (see yield stresses in uniaxial compression $\sigma_2 = 0$ and in uniaxial tension $\sigma_1 = 0$, respectively). Experimental finding in Konyashin (2014) displays similar tendencies: in compression the yield stress decreases linearly with the binder content, whereas in tension it remains almost independent of the binder content for average size WC grains. In

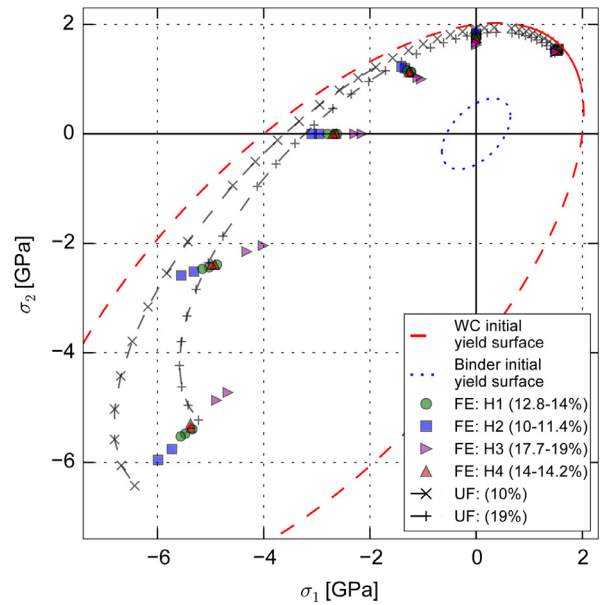


Fig. 9. Initial yield stresses for different microstructures obtained for different loading paths. Points are obtained from finite-element simulations with nine studied microstructures. The curves with line-points are constructed with the uniform field model, with respectively 10% and 19% binder content. Yield surfaces of WC and the binder are also plotted for convenience of comparison.

compressive and shear loading cases the major contribution to the accumulation of the effective plastic strain is made by the binder phase.

5.6. Distribution of strains and stresses

Due to the complex morphology of WC hardmetals, it is of interest to study not only the average response of the RVE, but also the local strain localization patterns shaped by the composite morphology. Results obtained with all investigated models both qualitatively and quantitatively are similar to those presented in this

Table 6
Initial yield stresses determined using FE simulations for 9 investigated microstructures and predicted by the UF model, in absence of TRS. Results are sorted by binder content.

Binder [area %]	Model	Equibiaxial compression [GPa]			Biaxial compression [GPa]			Uniaxial compression [GPa]		
		FE	UF	Δ[%]	FE	UF	Δ[%]	FE	UF	Δ[%]
10.0	H2-2	-5.99	-6.43	7.35	-5.55	-6.74	21.5	-3.10	-3.61	16.5
11.4	H2-1	-5.73	-6.23	8.73	-5.31	-6.55	23.4	-2.96	-3.55	19.9
12.8	H1-2	-5.56	-6.03	8.45	-5.16	-6.36	23.3	-2.80	-3.49	24.6
13.0	H1-1	-5.48	-6.00	9.49	-5.03	-6.33	25.8	-2.66	-3.48	30.8
14.0	H1-3	-5.34	-5.87	9.93	-4.88	-6.20	27.1	-2.62	-3.44	31.3
14.0	H4-1	-5.38	-5.87	9.11	-4.92	-6.20	27.1	-2.64	-3.44	30.3
14.2	H4-2	-5.38	-5.84	8.55	-4.98	-6.18	24.1	-2.70	-3.43	27.0
17.7	H3-2	-4.89	-5.39	10.2	-4.32	-5.73	32.6	-2.29	-3.28	43.2
19.0	H3-1	-4.68	-5.23	11.8	-4.01	-5.57	38.9	-2.15	-3.23	50.2

Binder [area %]	Model	Shear [GPa]			Uniaxial tension [GPa]			Equibiaxial tension [GPa]		
		FE	UF	Δ[%]	FE	UF	Δ[%]	FE	UF	Δ[%]
10.0	H2-2	-1.41	-1.57	11.3	1.83	1.91	4.4	1.55	1.54	0.65
11.4	H2-1	-1.34	-1.55	15.7	1.81	1.90	5.0	1.54	1.53	0.65
12.8	H1-2	-1.30	-1.52	16.9	1.77	1.88	6.2	1.53	1.52	0.66
13.0	H1-1	-1.23	-1.52	23.6	1.77	1.88	6.2	1.53	1.52	0.66
14.0	H1-3	-1.22	-1.50	22.9	1.74	1.87	7.5	1.52	1.52	0.30
14.0	H4-1	-1.23	-1.50	21.9	1.75	1.87	6.8	1.53	1.52	0.65
14.2	H4-2	-1.27	-1.49	20.2	1.74	1.87	7.5	1.53	1.51	0.66
17.7	H3-2	-1.10	-1.43	30.0	1.66	1.83	10.3	1.50	1.49	0.67
19.0	H3-1	-1.04	-1.41	35.6	1.62	1.82	12.4	1.49	1.48	0.68

section, therefore, could be seen as generic for WC hardmetals of similar type. Results obtained with the “H1-3” model are presented in this section.

Stress and strain maps and distribution histograms are shown in Figs. 10–12 for biaxial compression, shear and uniaxial tension loadings. Shown maps and histograms correspond to the moment when the effective equivalent plastic strain (\bar{p}) reaches 0.1%, i.e. the onset of plasticity for the effective behavior.

For biaxial compression the von Mises stress, pressure and equivalent plastic strain maps are shown in Fig. 10(a), (c) and (e), respectively. Distribution histograms of von Mises stress and pressure are shown in Figs. 10(b) and (d), respectively. For shear loading the same results are shown in Fig. 11. For uniaxial tension the same results are shown in Fig. 12. Supplementary information illustrating stress state of the material in the form of stress probability clouds in pressure-von Mises stress space is shown in Figs. 10(f), 11(f) and 12(f) for the three above-mentioned loading cases. The color of each point in the stress probability cloud shows the probability in % to find a point in the corresponding stress interval.

5.7. Thermal residual stress

The thermal expansion coefficient of the binder material is approximately 2.5 times higher than that of the tungsten carbide. In cooling from sintering to the room temperature, such difference results in appearance of compressive stresses within the WC grains' bulk and tensile stresses in the binder, as well as at the WC grains' edges, adjacent to the binder pools). Pressure distribution after thermal contraction is shown in Fig. 13 for “H1-3” model. This map was obtained for temperature independent elastic, plastic and thermal properties for cooling from 800 °C to 20 °C in 100 increments to account for plastic flow. Mean pressure in the WC phase is 209 MPa (compression) and -1265 MPa (tension) in the binder phase. These FE simulations results comply qualitatively with results of other studies (see, e.g., Spiegler and Fischmeister, 1992; Weisbrook and Krawitz, 1996; Mari et al., 2015).

During thermal contraction, while the effective stress remains zero, the forces exerted by each phase must be balanced

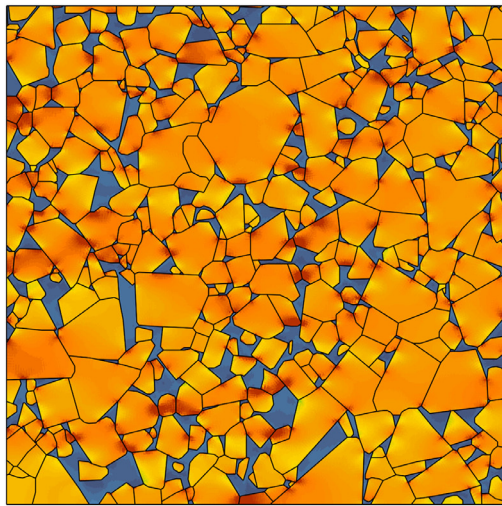
(Hutchings et al., 2005; Noyan and Cohen, 2013). For pressure in WC hardmetal composite that reads:

$$f_{WC}\bar{P}_{WC} + f_B\bar{P}_B = 0, \quad (25)$$

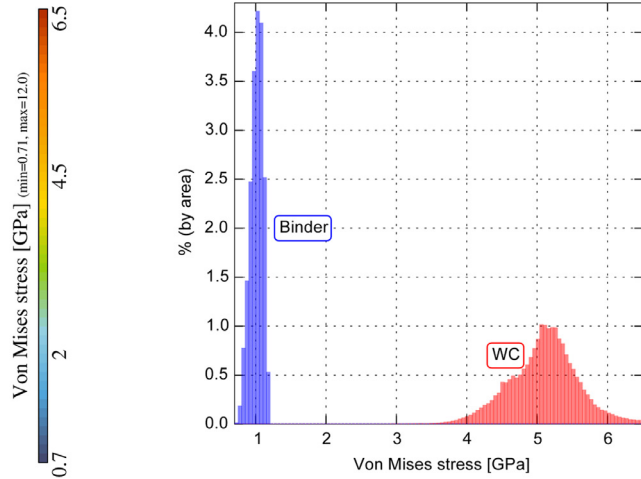
where f_i and \bar{P}_i are the volume fraction and the average pressure of the “ i ”th phase, respectively. Stress state of both phases upon completion of thermal contraction is shown in the form of a stress probability cloud in Fig. 14. It is beneficial for the WC phase to be in a compressive state after sintering, since it can then sustain higher tensile loads. However, pressures developed after sintering extend from compressive up to ≈ -500 MPa tensile (see Fig. 13(b)). This finding is in agreement with experimental data from Krawitz et al. (1988), where both compressive and tensile stresses in WC phase were also shown using neutron diffraction. Later, when hardmetal is in operation, tensile stresses can arise either locally, due to sliding contact with the rock, or due to composite's internal morphological particularities.

Distribution of equivalent plastic strains upon completion of thermal contraction is shown in Fig. 15. No plastic deformation is accumulated in the WC phase during this process, but the effective equivalent plastic strain level exceeds the threshold of 0.1%. It is the binder's post-yield hardening behavior that, for the most part, is partaking in the defining of effective composite response when loadings are applied after the thermal contraction. Hardmetals used in percussive drilling mostly experiences compressive loads and thus, it can be predicted that the larger the capacity of the binder to accumulate plastic deformation the longer the cohesion of hardmetal retains. The investigation of the effect of thermal residual stresses (TRS) on yield stress of WC-Co hardmetals can also be found in Litoshenko (2002).

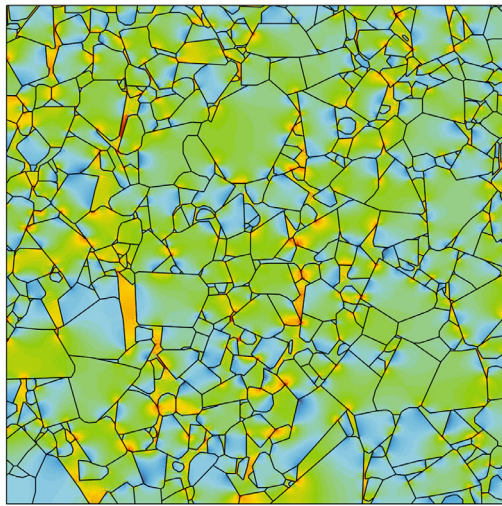
After thermal contraction interfaces between WC grains and pools of binder are predominantly in the tension state (see Fig. 13(a)). This suggests that these interfaces can act as sources of crack initiation. Interfaces between neighboring WC grains are in compression and at the corners of WC grain-WC grain contact compressive stresses are even higher, than along the interface edge. This suggests that these interfaces are more secured from becoming a source of crack initiation. These findings are in agreement with the study Weisbrook and Krawitz (1996). A study of the



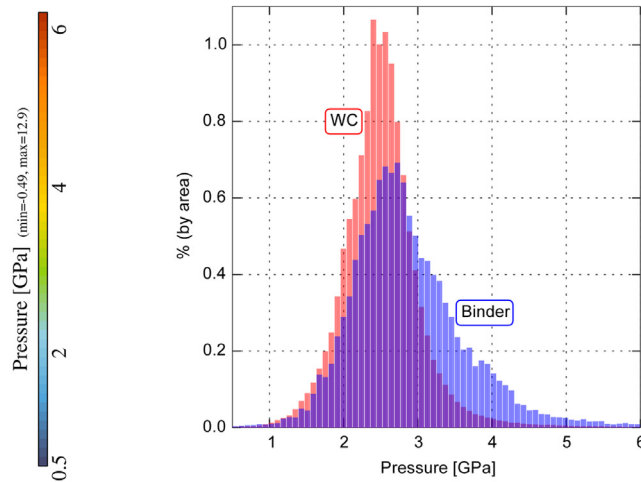
(a)



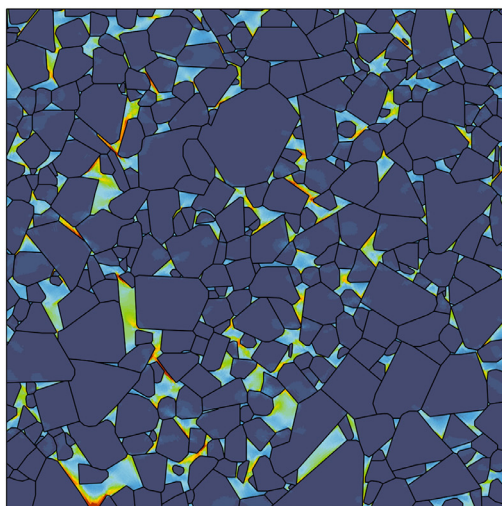
(b)



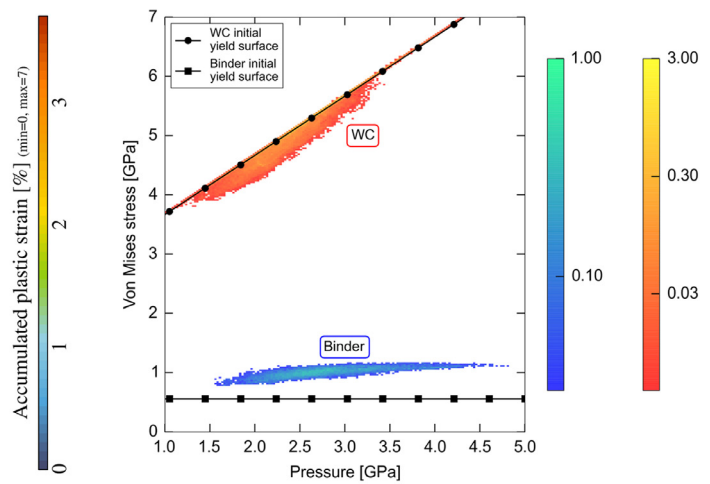
(c)



(d)



(e)



(f)

Fig. 10. Illustration of the state of “H1-3” model in biaxial compression loading at reaching the initial “yield surface” ($\bar{p} = 0.1\%$). Figures correspond to von Mises stress (a,b); pressure (c,d); equivalent plastic strain (e); stress probability cloud in pressure-von Mises stress space for the WC phase and the binder phase (f). Color-bars in (f) show the probability (in %) to find a point at a current location in stress space (logarithmic color scale). The size of each “bin” is $[250 \times 250]$ MPa². (For interpretation of the references to color in this figure legend, the reader is referred to the web version of this article.)

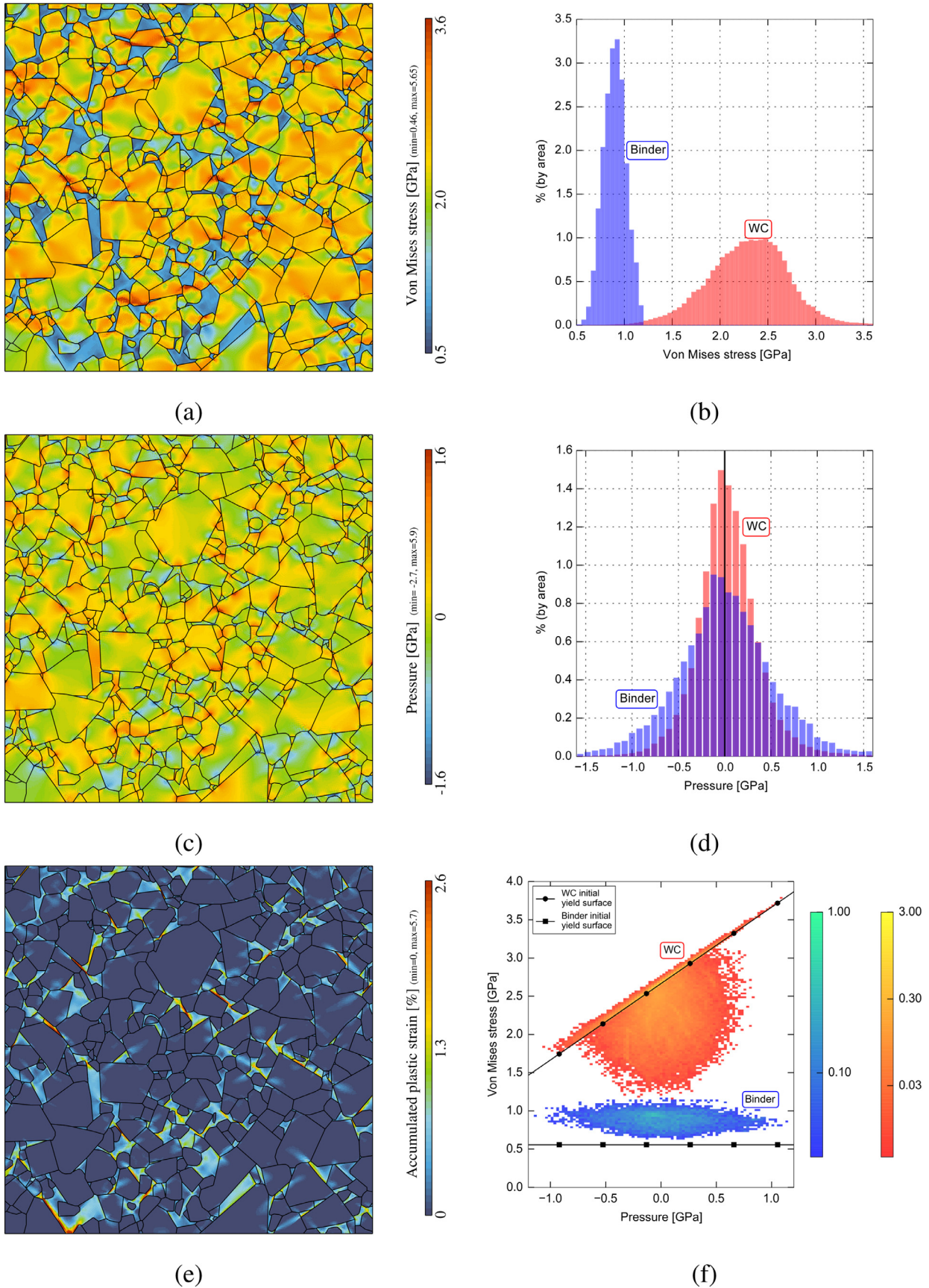


Fig. 11. Illustration of the state of “H1-3” model in shear loading (compressive loading is in horizontal direction) at reaching the initial “yield surface” ($\bar{p} = 0.1\%$). Figures correspond to von Mises stress (a,b); pressure (c,d); equivalent plastic strain (e); stress probability cloud in pressure-von Mises stress space for the WC and the binder phases (f). Color-bars in (f) show the probability (in %) to find a point at a current location in stress space (logarithmic color scale). The size of each “bin” is $[250 \times 250]$ MPa². (For interpretation of the references to color in this figure legend, the reader is referred to the web version of this article.)

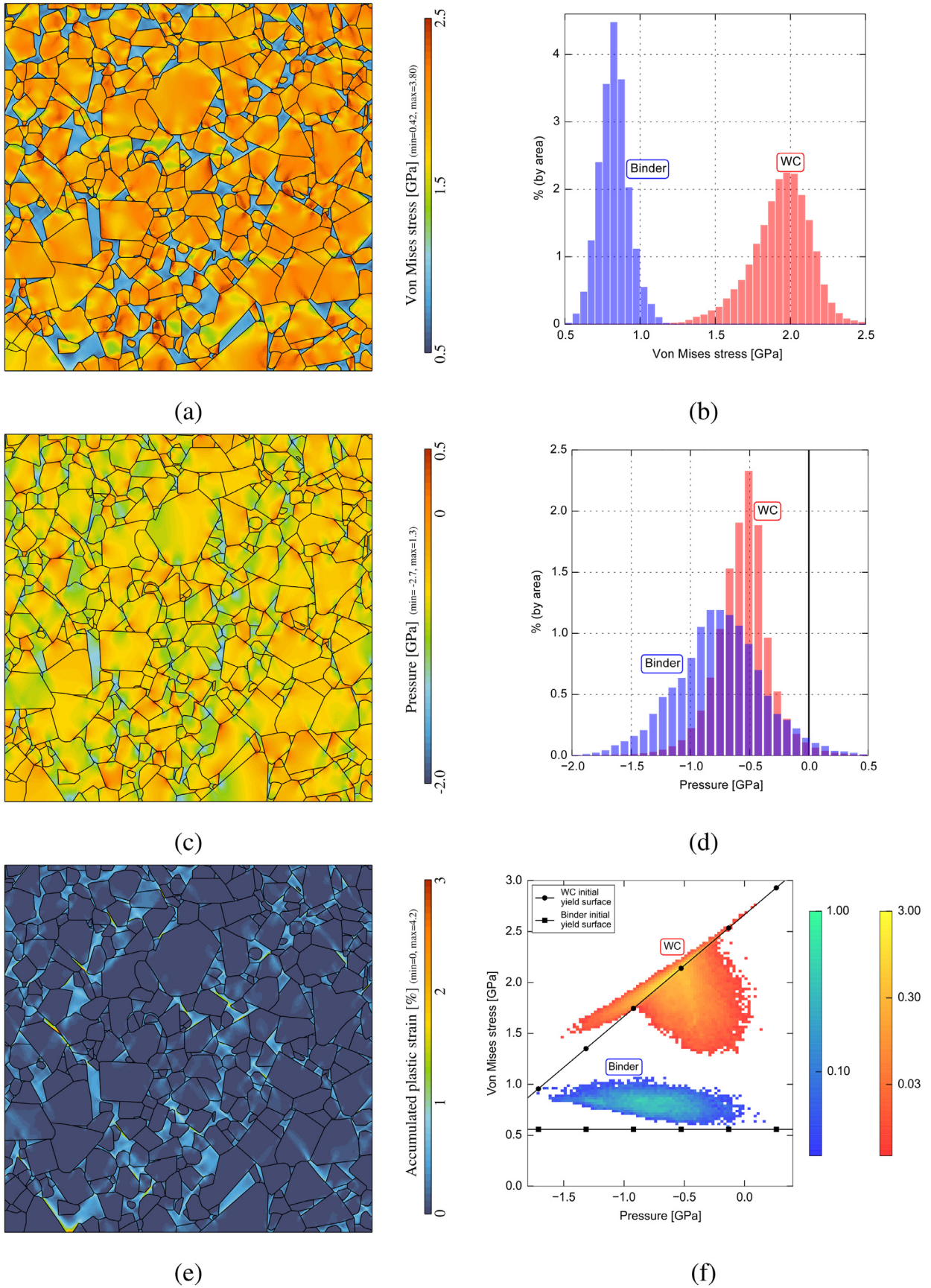


Fig. 12. Illustration of the state of “H1-3” model in uniaxial tension loading (compressive loading is in horizontal direction) at reaching the initial “yield surface” ($\bar{p} = 0.1\%$). Figures correspond to von Mises stress (a,b); pressure (c,d); equivalent plastic strain (e); stress probability cloud in pressure-von Mises stress space for the WC phase and the binder phases (f). Color-bars in (f) show the probability (in %) to find a point at a current location in stress space (logarithmic color scale). The size of each “bin” is $[250 \times 250]$ MPa². (For interpretation of the references to color in this figure legend, the reader is referred to the web version of this article.)

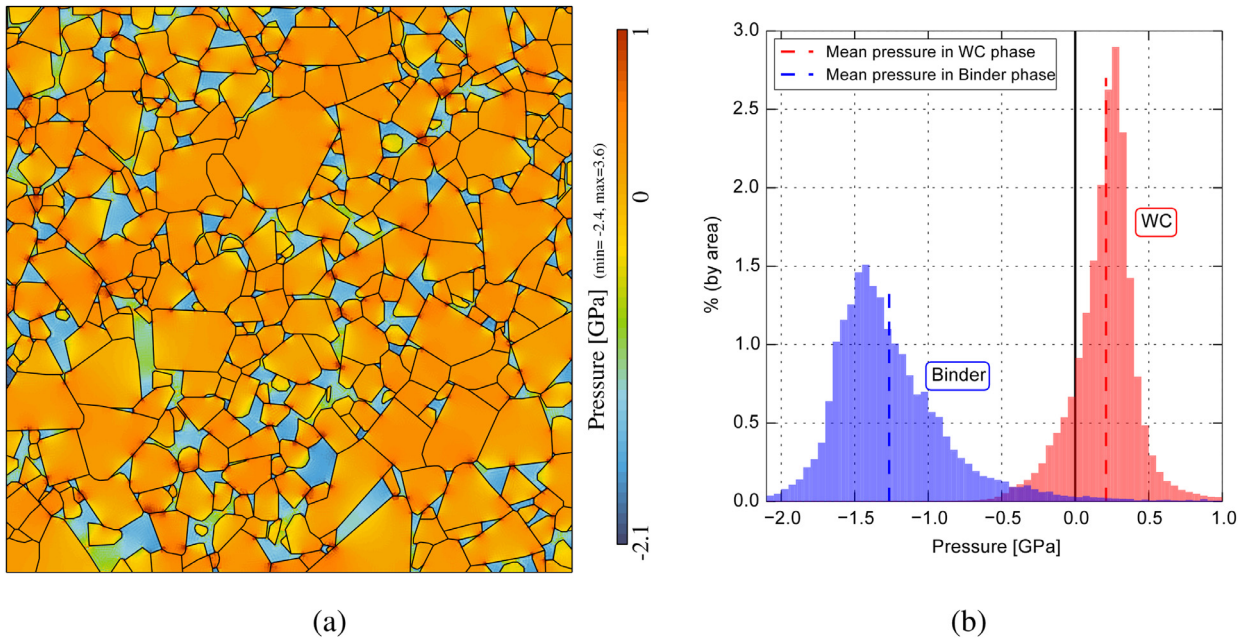


Fig. 13. Pressure distribution after thermal contraction from 800 °C to 20 °C for “H1-3” model: pressure distribution map (a) and distribution histogram (b). (For interpretation of the references to color in this figure legend, the reader is referred to the web version of this article.)

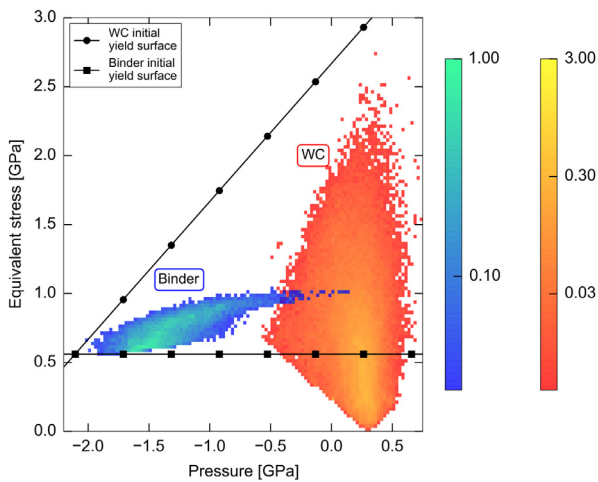


Fig. 14. Stress state upon completion of thermal contraction from 800 °C to 20 °C for “H1-3” model. Two-dimensional histogram in pressure-von Mises stress space for WC and binder phases. Color-bars shows the probability in % to find a point at a current location in stress space (logarithmic color scale). The size of each “bin” is $[250 \times 250]$ MPa². (For interpretation of the references to color in this figure legend, the reader is referred to the web version of this article.)

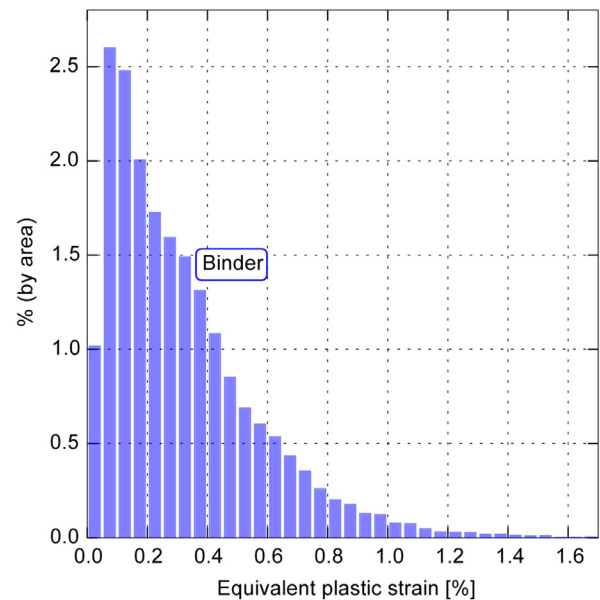


Fig. 15. Distribution of equivalent plastic strains upon completion of thermal contraction from 800 °C to 20 °C for “H1-3” model. No plastic deformation is accumulated in the WC phase during this simulation.

effect of TRS on the fracture toughness of WC-Co can be found in [Cutler and Virkar \(1985\)](#).

It is of interest to see how the stress state changes in phases when the material with pre-existing TRS is loaded. Three types of loadings were applied on “H1-3” FE model, which was taken with zero initial (thermal residual) stresses and with simulated TRS. Pressure and von Mises stress distribution histograms are shown for biaxial compression, shear and uniaxial tension loadings in [Fig. 16](#). Unshaded bars show the stress state after thermal contraction, but prior to application of the loadings. These histograms can be compared with those shown in [Figs. 10\(d\)](#), [Fig. 11\(d\)](#) and [Fig. 12\(d\)](#). Spatial distribution of residual stresses in cemented WC-10 wt%Co hardmetal was also computed using a finite-element model in [Spiegler and Fischmeister \(1992\)](#), where a 2D model with

20 WC grains was used, but, nevertheless, stress distributions show a very close resemblance to the results of the current study.

As shown in [Fig. 16](#), a single-peak stress distributions prior to the application of loadings converts to a double peak when loaded. This effect is absent in the binder distribution under uniaxial tension (see [Fig. 16\(c\)](#)), since most of the binder is already in the tension upon completion of thermal contraction.

5.8. Parameters sensitivity

As indicated in [Table 2](#), different binder materials are used for different grades, whereas in our models we restricted the study to a particular binder, cobalt. Thus, it is of interest to investigate the

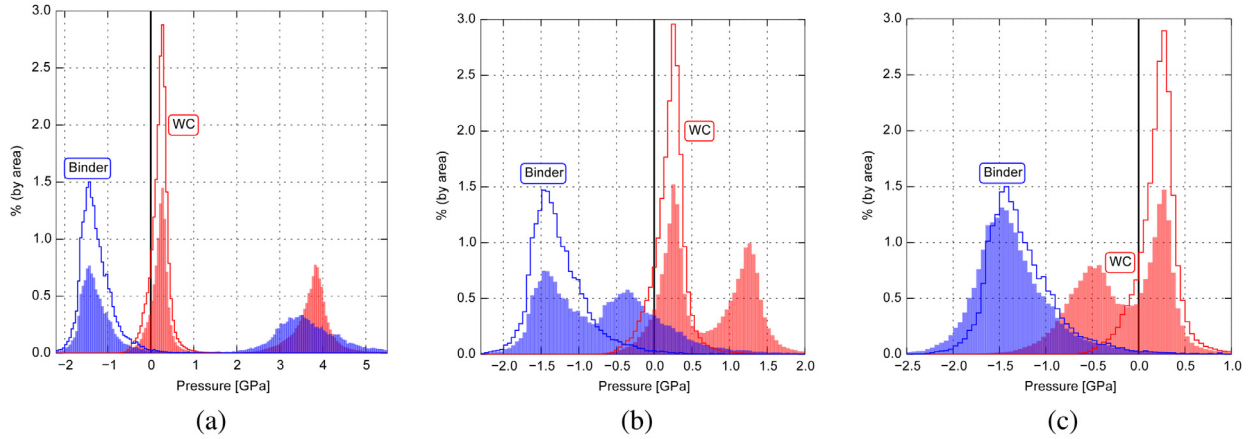


Fig. 16. Pressure distribution histograms for “H1-3” model after biaxial compression (a), shear (b) and uniaxial tension (c) with TRS. Unshaded bars show the stress state after thermal contraction, but prior to application of the loading.

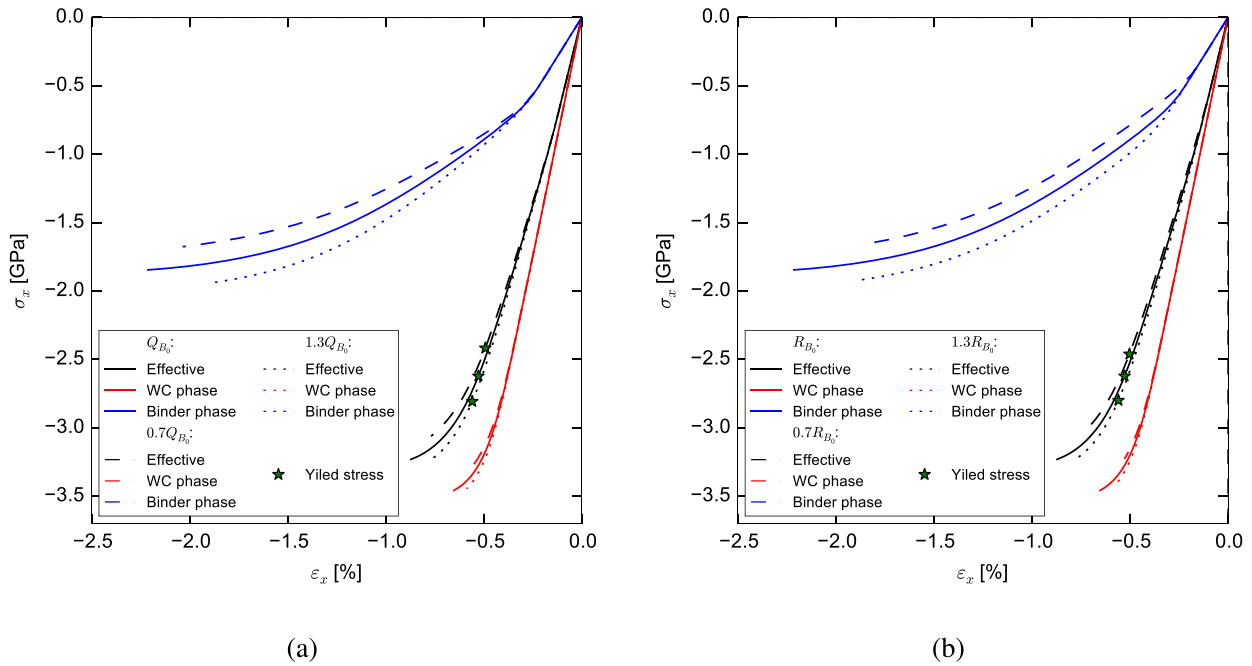


Fig. 17. Sensitivity of the “H1-3” model under uniaxial compression to changes in (a) the initial binder yield stress R_{B_0} and (b) the binder hardening parameter Q_B , star markers denote yield stresses determined at 0.1% of effective equivalent plastic strain.

influence of the binder material properties variation on the effective response of the WC hardmetal. Three studies were performed using FE “H1-3” model: (i) binder material initial yield stress R_{B_0} (in Eq. (6)) was raised and lowered by 30%, (ii) binder material hardening parameter Q_B (in Eq. (6)) was raised and lowered by 30% and (iii) the coefficient of thermal expansion difference between WC and binder phase was changed. All other material properties of both phases are kept the same. Sensitivity of “H1-3” model response to these variations in binder properties is shown in Fig. 17 for the case of uniaxial compression loading. Since the binder fraction is relatively small (14% for the considered sample), the effective response being counterbalanced by the WC behavior, changes slightly: for example, the yield stress in compression (evaluated at 0.1% of effective equivalent plastic strain) changes in the interval $\pm 5 - 6\%$ around the original yield stress. Dependence of the mean residual pressure in WC and binder phases after thermal contraction with respect to the ratio of their CTE is given in Table 7 for 5 different α_B/α_{WC} ratios.

Table 7

Dependence of the mean residual pressure in phases on the ratio of WC and binder thermal expansion coefficients, obtained using FE simulations with “H1-3” model for cooling from 800° to 20°. The reference case corresponds to $\alpha_B/\alpha_{WC}=2.5$ (see Table 1).

α_B/α_{WC}	Mean pressure in binder phase [MPa]	Mean pressure in WC phase [MPa]
3.5	-1845.1	305.6
3.0	-1587.0	262.4
2.5	-1265.5	209.2
2.0	-907.0	149.8
1.5	-499.4	82.2

5.9. Uniform field model in 3D

As shown in Sections 5.4 and 5.5, the uniform field model gives a good prediction of 2D WC hardmetal behavior up to reaching the yield surface. Thus, it can be readily used to obtain results for 3D

Table 8

Elastic moduli, coefficients of thermal expansion and yield stresses in compression and tension for the 3D UF model with different binder content.

Binder volume fraction [%]	Young's modulus [GPa]	Poisson's ratio	Coefficient of thermal expansion, Eq. (26)) [$10^{-6}/K$]	Yield stress in uniaxial compression [GPa]	Yield stress in uniaxial tension [GPa]
4	677.7	0.201	5.39	−3.88	1.97
6	662.8	0.203	5.49	−3.80	1.95
8	648.2	0.205	5.59	−3.72	1.93
10	633.7	0.207	5.70	−3.64	1.90
12	619.4	0.209	5.81	−3.57	1.88
14	605.2	0.211	5.92	−3.49	1.86
16	591.2	0.213	6.04	−3.41	1.83
18	577.5	0.215	6.16	−3.34	1.81
20	563.9	0.217	6.28	−3.26	1.78

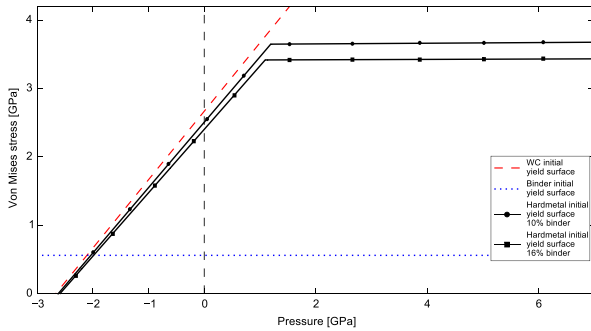


Fig. 18. Yield surface obtained for 10% and 16% of binder volume fraction using 3D uniform field model with spherical inclusions.

case. In order to obtain elastic moduli, coefficient of thermal expansion and yield surface of WC hardmetal in 3D case we used a uniform field model constructed for a spherical inclusion problem. The Eshelby tensor is taken in the form shown in Eq. (16).

Elastic moduli were determined using results of uniaxial compression simulations for different binder volume fractions. Coefficients of thermal expansion were determined using results of thermal contraction simulations. Elastic moduli, coefficients of thermal expansion and the yield stresses in compression and tension are given in Table 8 for different binder volume fractions. The effective coefficient of thermal expansion is computed using the following equation (Zaoui, 1997):

$$\alpha_{\text{eff}} = \langle \alpha \rangle + \frac{1/K_{\text{eff}} - \langle 1/K \rangle}{1/K_1 - 1/K_2} (\alpha_1 - \alpha_2), \quad (26)$$

where $\langle x \rangle = f_1 x_1 + (1 - f_1) x_2$ denotes the weighted mean value, with f_1 be the volume fraction of phase 1, K is the bulk modulus, which for isotropic material can be expressed through Young's modulus and Poisson's ratio as $K = E/(3(1 - 2\nu))$, and K_{eff} is its homogenized value.

The effective yield surfaces obtained for 10% and 16% of binder volume fractions are shown in Fig. 18 in pressure-von Mises stress space. Such presentation is sufficient, since the shape of the effective yield surface does not depend on the third stress invariant. The yield surface shape could be represented as a combination of linear Drucker–Prager and von Mises yield surfaces. The yield stress in hydrostatic tension for linear Drucker–Prager part is ≈ 2.65 GPa and the friction angle is $\approx 44^\circ$. The yield stress for the von Mises part is ≈ 3.4 GPa for $f_B = 16\%$ and ≈ 3.65 GPa for $f_B = 10\%$. The linear Drucker–Prager part follows closely the Drucker–Prager criterion of WC, whereas the composite “von Mises part” is about six times higher than the von Mises criterion of the binder.

6. Conclusions

Nine two-dimensional finite element (FE) models were created based on SEM images of four different WC hardmetal grades in order to investigate the effective thermo-mechanical behavior of this composite. Created models are $19.5 \times 19.5 \mu\text{m}^2$ in size, with the binder content varying from 10% to 19% by area fraction. Number of WC grains contained in each model varies between 340 and 490 grains. A pressure-dependent non-associated plastic behavior (Drucker–Prager criterion) was used for the WC phase and the von Mises criterion for the binder phase. Isotropic linear elasticity is used for both phases.

We computed effective elastic moduli and coefficients of thermal expansion using a homogenization method based on the FE analysis of representative elementary volumes. Six characteristic loadings in 2D principal stress space were applied to the RVE to determine the effective yield stresses for every path. A generalized plain strain (“2.5D”) FE formulation was used enabling to allow a non-zero out-of-plane stresses in each phase, while keeping zero the average effective stress. Due to the two-dimensional nature of the simulations, the resulting effective material is transversely isotropic. Constructed FE model and the choice of material models for constituents allows to qualitatively reproduce the mechanical response of WC hardmetal under various loadings both in elastic and plastic regimes. In addition, it provides us with local stress fields, i.e. the stress statistics, which is critical for understanding and predicting onsets of fracture and wear.

A uniform field (UF) elasto-plastic model constructed for cylindrical and spherical inclusion problems was implemented for the WC hardmetal two-phase composite. Comparison is made between the 2.5D FE model and the UF model for cylindrical inclusions. Predictions of the two approaches for nine studied microstructures differ by less than 1% for in-plane Young's modulus and Poisson's ratio, and by less than 0.25% for the out-of-plane constants. This good agreement indicates that the constructed FE models are representative. The effective in-plane Young's modulus follows closely the upper Hashin–Shtrikman bound. For a binder content 10% to 20%, a linear decrease of the Young's modulus with respect to the binder fraction can be assumed with a high accuracy. The corresponding slope is determined by the mean slope of the upper Hashin–Shtrikman bound. The effective in-plane and out-of-plane coefficients of thermal expansion computed according to the FE and UF models differ by less than 2%.

Outside the elastic domain, the UF model is also able to predict quite accurately the deformation curves in case of moderate loads. However, because of a high dispersion of local stresses around the mean value, the yield stresses predicted by the UF model is significantly higher than those predicted by the full-field FE model. Moreover, this difference is amplified by the fact that the elasto-plastic UF model was formulated using constant plastic accommo-

dition, which is known to result in an overestimation of residual stresses between phases. A more elaborated UF model reformulated in a rate form or a β model would produce more accurate results. The discrepancy error in the yield stresses evaluated at 0.1% of effective plastic strain is low in equibiaxial tension (the error is less than 1%). It is higher for the other loading types like equibiaxial compression, asymmetric biaxial compression and one-dimensional compression. It is worth noting that the error is under control for low binder content (around 10%, with a maximum of 20% for the unsymmetric biaxial compression). It is higher (reaching 50%) for large binder content (19%) and one-dimensional compression. The fact that the yield stress differs in both models is not critical for the agreement of the average behavior of the materials: as hardening is very stiff, the curves are very close to each other at the onset of plastic flow, so that the FE and UF model are in good agreement for all considered loads.

The satisfactory agreement between the FE and UF models for the 2.5D case confirms the validity of the UF model for WC hardmetals with its specific microstructure and material behaviors. Thus, we constructed a UF model for a spherical inclusion problem. Similar to the 2D case, in elasticity we obtain a quasi-linear decrease in the effective Young's modulus with the binder content. In elasto-plastic regime, the yield surface obtained with this UF model consists of two branches distinguishable in the pressure–von Mises stress space. The first branch is a Drucker–Prager cone with the friction angle slightly smaller than the original friction angle of the WC, and which increases with the increasing binder content. The second branch is the von Mises branch, parallel to the pressure axis. A sharp transition between the two branches is predicted by the UF model. In prospective, it is planned to verify this result using a three-dimensional FE model. The obtained yield surface gives a reasonable difference between yield stresses in uniaxial compression and tension; it also predicted, for the increasing binder content, a more significant decrease of the yield stress in compression than in tension, which is in agreement with experimental data.

This study was complemented by a weakly-coupled thermo-mechanical analysis of hardmetal behavior during thermal contraction using finite element models. In cooling from sintering temperatures to the room temperature (from 800 °C to 20 °C), high stresses develop in the composite due to the difference in coefficients of thermal expansion of the WC and the binder. These stresses influence considerably the mechanical behavior of the composite and cannot be taken into account directly within UF models based on Eshelby's solution for a solitary inclusion. Even if thermal stresses could be included in a UF model, the finite element tests presented here demonstrate that under mechanical loading in presence of residual thermal stresses, the total stresses form a probability distributions with two peaks, for which the notion of the mean value becomes irrelevant.

We conclude that a uniform field model can be used with a high confidence to estimate the average mechanical behavior of WC hardmetals under moderate loads both in elastic regime and at the onset of plastic flow. However, for predicting extreme phenomena like wear and fracture, which are governed not by mean stress values but rather by the tail of the probability distributions, more accurate homogenization models are needed, which would also include in consideration the dispersion of local stresses (see, e.g., the recent works [Fritzen and Leuschner, 2013](#); [Michel and Suquet, 2016](#)).

Acknowledgment

The authors would like to acknowledge the support from The Research Council of Norway through the knowledge building project KPN 216436 (“Numerical-experimental technology platforms for cost-effective deep hard rock drilling”). Sandvik is ac-

knowledged for the supply of WC hardmetal drill-bit buttons used in the current investigation. The authors are also grateful to Djamel Missoum-Benziane and Nikolay Osipov for their help with finite-element simulations.

References

- Almond, E., 1983. Deformation Characteristics and Mechanical Properties of Hardmetals. In: *Science of Hard Materials*. Springer, pp. 517–561.
- Almond, E., Roebuck, B., 1988. Identification of optimum binder phase compositions for improved WC hard metals. *Mater. Sci. Eng.: A* 105, 237–248.
- Andr n, H.-O., 2001. Microstructures of cemented carbides. *Mater. Des.* 22 (6), 491–498.
- Barbe, F., Decker, L., Jeulin, D., Cailletaud, G., 2001a. Intergranular and intragranular behavior of polycrystalline aggregates. part 1: FE model. *Int. J. Plast.* 17 (4), 513–536.
- Barbe, F., Forest, S., Cailletaud, G., 2001b. Intergranular and intragranular behavior of polycrystalline aggregates. part 2: results. *Int. J. Plast.* 17 (4), 537–563.
- Belteridge, W., 1982. Cobalt and Its Alloys. John Wiley & Sons.
- Benzergha, A., Besson, J., Pineau, A., 1999. Coalescence-controlled anisotropic ductile fracture. *Trans. ASME, J. Eng. Mater. Technol.* 121, 221–229.
- Berryman, J.G., 1980. Long-wavelength propagation in composite elastic media II. ellipsoidal inclusions. *J. Acoust. Soc. Am.* 68 (6), 1820–1831.
- Berryman, J.G., 1992. Single-scattering approximations for coefficients in Biot's equations of poroelasticity. *J. Acoust. Soc. Am.* 91 (2), 551–571.
- Berveiller, M., Zaoui, A., 1979. An extension of the self-consistent scheme to plastically flowing polycrystal. *J. Mech. Phys. Solids* 26, 325–344.
- Besson, J., Cailletaud, G., Chaboche, J.-L., Forest, S., 2009. *Non-linear Mechanics of Materials*, 167. Springer Science and Business Media.
- Besson, J., Foerch, R., 1997. Large scale object-oriented finite element code design. *Comput. Methods Appl. Mech. Eng.* 142 (1), 165–187.
- Beste, U., Hartzell, T., Engqvist, H., Ax n, N., 2001. Surface damage on cemented carbide rock-drill buttons. *Wear* 249 (3), 324–329.
- Beste, U., Jacobson, S., 2008a. A new view of the deterioration and wear of WC–Co cemented carbide rock drill buttons. *Wear* 264 (11), 1129–1141.
- Beste, U., Jacobson, S., 2008b. Targeting micro-sectioning – a technique to study sub-surface features in worn specimens. *Wear* 264 (11), 1152–1156.
- Beste, U., Jacobson, S., Hogmark, S., 2008. Rock penetration into cemented carbide drill buttons during rock drilling. *Wear* 264 (11), 1142–1151.
- Borgh, I., Hedstr m, P., Odqvist, J., Borgenstam, A.,  gren, J., Gholinia, A., Winiarski, B., Withers, P.J., Thompson, G.E., Mingard, K., et al., 2013. On the three-dimensional structure of WC grains in cemented carbides. *Acta Mater.* 61 (13), 4726–4733.
- Bornert, M., Bretheau, T., Gilormini, P., 2001a. Homog nisation En M canique Des Mat riaux, Tome 1: Mat riaux Al atoires  lastiques Et Milieux P riodiques. Hermes Science.
- Bornert, M., Bretheau, T., Gilormini, P., 2001b. Homog nisation En M canique Des Mat riaux, Tome 2: Comportements Non Lin aires Et Probl mes Ouverts. Hermes Science.
- Budiansky, B., Wu, T., 1961. Theoretical prediction of plastic strains of polycrystals. Technical Report. DTIC Document.
- Cailletaud, G., Coudon, F., 2016. Scale transition rules applied to crystal plasticity. In: Trovalusci, P. (Ed.), *Materials with Internal Structure: Multiscale and Multifield Modeling and Simulation*. Springer International Publishing, pp. 1–15.
- Cailletaud, G., Forest, S., Jeulin, D., Feyel, F., Galliet, I., Mounoury, V., Quilici, S., 2003. Some elements of microstructural mechanics. *Comput. Mater. Sci.* 27, 351–374.
- Cailletaud, G., Pilvin, P., 1994. Utilisation de mod les polycristallins pour le calcul par  l ments finis. *Revue Europ enne des  l ments Finis* 3 (4), 515–541.
- Casta eda, P.P., 1991. The effective mechanical properties of nonlinear isotropic composites. *J. Mech. Phys. Solids* 39 (1), 45–71.
- Chabretou, V., Allibert, C., Missiaen, J., 2003. Quantitative analysis of the effect of the binder phase composition on grain growth in WC–Co sintered materials. *J. Mater. Sci.* 38 (12), 2581–2590.
- Chawla, N., Patel, B., Koopman, M., Chawla, K., Saha, R., Patterson, B., Fuller, E., Langer, S., 2002. Microstructure-based simulation of thermomechanical behavior of composite materials by object-oriented finite element analysis. *Mater. Charact.* 49 (5), 395–407.
- Chermant, J., Osterstock, F., 1976. Fracture toughness and fracture of WC–Co composites. *J. Mater. Sci.* 11 (10), 1939–1951.
- Csan di, T., B'anda, M., Duszov , A., Chinh, N.Q., Szommer, P., Dusza, J., 2014. Deformation characteristics of WC micropillars. *J. Eur. Ceram. Soc.* 34 (15), 4099–4103.
- Cutler, R.A., Virkar, A.V., 1985. The effect of binder thickness and residual stresses on the fracture toughness of cemented carbides. *J. Mater. Sci.* 20 (10), 3557–3573.
- Doi, H., Fujiwara, Y., Miyake, K., Osawa, Y., 1970. A systematic investigation of elastic moduli of WC–Co alloys. *Metallur. Mater. Trans.* 1 (5), 1417–1425.
- Drake, E., Krawitz, A., 1981. Fatigue damage in a WC–Nickel cemented carbide composite. *Metall. Trans. A* 12 (3), 505–513.
- El Houdaigui, F., Forest, S., Gourgues, A., Jeulin, D., 2007. On the size of the representative volume element for isotropic elastic polycrystalline copper. In: *IUTAM Symposium on Mechanical Behavior and Micro-Mechanics of Nanostructured Materials*. Springer, pp. 171–180.
- Eshelby, J., 1957. The determination of the elastic field of an ellipsoidal inclusion, and related problems 241, 376–396.

- Exner, H., 1979. Physical and chemical nature of cemented carbides. *Int. Met. Rev.* 24 (1), 149–173.
- Exner, H., Gurland, J., 1970. A review of parameters influencing some mechanical properties of tungsten carbide–cobalt alloys. *Powder Metall.* 13 (25), 13–31.
- Fang, Z.Z., Koopman, M.C., 2014. Cemented tungsten carbide hardmetal – an introduction. In: Sarin, V., Mari, D., Llanes, L. (Eds.), *Comprehensive Hard Materials*. Volume I. Newnes, pp. 123–138. 1.04.
- Felgar, R., Lubahn, J., 1957. Mechanical behavior of cemented carbides. In: *Proceedings ASTM*, pp. 770–790.
- Fernandes, C., Senos, A., 2011. Cemented carbide phase diagrams: a review. *Int. J. Refract. Met. Hard Mater.* 29 (4), 405–418.
- Fischmeister, H.F., 1983. Conference key note paper development and present status of the science and technology of hard materials. In: *Science of Hard Materials*. Springer, pp. 1–45.
- French, D.N., 1969. X-Ray stress analysis of WC–Co cermets: II, temperature stresses. *J. Am. Ceram. Soc.* 52 (5), 271–275.
- Fritzen, F., Leuschner, M., 2013. Reduced basis hybrid computational homogenization based on a mixed incremental formulation. *Comput. Methods Appl. Mech. Eng.* 260, 143–154.
- Gille, G., Bredthauer, J., Gries, B., Mende, B., Heinrich, W., 2000. Advanced and new grades of WC and binder powder—their properties and application. *Int. J. Refract. Met. Hard Mater.* 18 (2), 87–102.
- Golovchan, V., Litoshenko, N., 2010. The stress–strain behavior of WC–Co hardmetals. *Comput. Mater. Sci.* 49 (3), 593–597.
- Gurland, J., 1979. A structural approach to the yield strength of two-phase alloys with coarse microstructures. *Mater. Sci. Eng.* 40 (1), 59–71.
- Gurland, J., Norton, J.T., 1952. Role of the binder phase in cemented tungsten carbide–cobalt alloys. *Trans. AIME* 194 (10), 1051–1056.
- Hall, E., 1951. The deformation and ageing of mild steel: III discussion of results. *Proc. Phys. Soc. Lond., Sect. B* 64 (9), 747.
- Hashin, Z., Shtrikman, S., 1962. A variational approach to the theory of the elastic behaviour of polycrystals. *J. Mech. Phys. Solids* 10 (4), 343–352.
- Henjered, A., Hellsing, M., Andrén, H.-O., Nordén, H., 1986. Quantitative microanalysis of carbide/carbide interfaces in WC–Co-base cemented carbides. *Mater. Sci. Technol.* 2 (8), 847–855.
- Herring, C., 1951. Some theorems on the free energies of crystal surfaces. *Phys. Rev.* 82 (1), 87.
- Hibbs, M., Sinclair, R., 1981. Room-temperature deformation mechanisms and the defect structure of tungsten carbide. *Acta Metall.* 29 (9), 1645–1654.
- Hill, R., 1965a. A self-consistent mechanics of composite materials. *J. Mech. Phys. Solids* 13, 213–222.
- Hill, R., 1965b. A self-consistent mechanics of composite materials. *J. Mech. Phys. Solids* 13 (4), 213–222.
- Hong, J., Gurland, J., 1983. A study of the fracture process of WC–Co alloys. In: *Science of Hard Materials*. Springer, pp. 649–669.
- Huet, C., 1990. Application of variational concepts to size effects in elastic heterogeneous bodies. *J. Mech. Phys. Solids* 38 (6), 813–841.
- Hutchings, M.T., Withers, P.J., Holden, T.M., Lorentzen, T., 2005. *Introduction to the Characterization of Residual Stress by Neutron Diffraction*. CRC Press.
- Ingelstrom, N., Nordberg, H., 1974. The fracture toughness of cemented tungsten carbides. *Eng. Fract. Mech.* 6 (3), 597–607.
- Jaansson, B.O., 1971. Residual stresses and stress-strain behaviour of the WC–Co composite material. *Mater. Sci. Eng.* 8 (1), 41–53.
- Jaansson, B.O., Sundström, B.O., 1972. Determination of young's modulus and poisson's ratio for WC–Co alloys by the finite element method. *Mater. Sci. Eng.* 9, 217–222.
- Jeulin, D., 2013. Random tessellations and boolean random functions. In: *Mathematical Morphology and Its Applications to Signal and Image Processing*. Springer, pp. 25–36.
- Jeulin, D., Ostoja-Starzewski, M., 2001. *Mechanics of Random and Multiscale Microstructures*. Springer.
- Kanit, T., Forest, S., Galliet, I., Mounoury, V., Jeulin, D., 2003. Determination of the size of the representative volume element for random composites: statistical and numerical approach. *Int. J. Solids Struct.* 40 (13), 3647–3679.
- Kim, C.-S., Massa, T.R., Rohrer, G.S., 2008. Interface character distributions in WC–Co composites. *J. Am. Ceram. Soc.* 91 (3), 996–1001.
- Kingman, J.F.C., 1992. *Poisson Processes*, 3. Oxford University Press.
- Kisi, E.H., Howard, C.J., et al., 2008. *Applications of Neutron Powder Diffraction*. Oxford University Press.
- Kolaska, H., 1992. The dawn of the hardmetal age. *Powder Metallur. Int.* 24 (5), 311–314.
- Konyashin, I., 2014. Cemented carbides for mining, construction and wear parts. In: Sarin, V., Mari, D., Llanes, L. (Eds.), *Comprehensive Hard Materials*. Volume I. Newnes, pp. 425–451. 1.15.
- Koopman, M., Chawla, K.K., Coffin, C., Patterson, B.R., Deng, X., Patel, B.V., Fang, Z., Lockwood, G., 2002. Determination of elastic constants in WC–Co metal matrix composites by resonant ultrasound spectroscopy (rus) and impulse excitation. *Adv. Eng. Mater.* 4 (1–2), 37–42.
- Koplik, J., Needleman, A., 1988. Void growth and coalescence in porous plastic solids. *Int. J. Solids Struct.* 24 (8), 835–853.
- Krawitz, A., Crapenhof, M., Reichel, D., Warren, R., 1988. Residual stress distribution in cermets. *Mater. Sci. Eng.* A 105, 275–281.
- Krawitz, A., Reichel, D., Hitterman, R., 1989. Residual stress and stress distribution in a WC–Ni composite. *Mater. Sci. Eng.* A 119, 127–134.
- Krawitz, A.D., 2001. *Introduction to Diffraction in Materials Science and Engineering*. Wiley.
- Krawitz, A.D., Drake, E.F., 2014. Residual stresses. In: Sarin, V., Mari, D., Llanes, L. (Eds.), *Comprehensive Hard Materials*. Volume I. Newnes, pp. 385–404.
- Kröner, E., 1961. Zur plastischen verformung des vielkristalls. *Acta Metall.* 9 (2), 155–161.
- Kröner, E., 1977. Bounds for effective moduli of disordered materials. *J. Mech. Phys. Solids* 25, 137–155.
- Kröner, E., 1981. Linear properties of random media – The systematic theory. In: Huet, C., Zaoui, A. (Eds.), *Comportements rhéologiques et structure des matériaux*. Editions ENPC, CR 15e Coll. GFR, pp. 15–40.
- Lay, S., Allibert, C., Christensen, M., Wahnström, G., 2008. Morphology of WC grains in WC–Co alloys. *Mater. Sci. Eng.* A 486 (1), 253–261.
- Lay, S., Missiaen, J.-M., 2014. Microstructure and morphology of hardmetals. In: Sarin, V., Mari, D., Llanes, L. (Eds.), *Comprehensive Hard Materials*. Volume I. Newnes, pp. 91–122. 1.03.
- Lee, H.-C., Gurland, J., 1978. Hardness and deformation of cemented tungsten carbide. *Mater. Sci. Eng.* 33 (1), 125–133.
- Lee, M., Gilmore, R., 1982. Single crystal elastic constants of tungsten monocarbide. *J. Mater. Sci.* 17 (9), 2657–2660.
- Lemaitre, J., Desmorat, R., 2005. *Engineering Damage Mechanics: Ductile, Creep, Fatigue and Brittle Failures*. Springer Science & Business Media.
- Litoshenko, N., 2002. Regularities of influence of residual thermal microstresses and dispersion of carbide grains sizes on the deformation characteristics of WC–Co hard metals. *Bakul Institute for Superhard Materials of the National Academy of Science of Ukraine, Kyiv Ph.D. thesis*.
- Lueth, R.C., 1972. Study of the strength of tungsten carbide–cobalt alloys from a fracture mechanics viewpoint. *Michigan State University Ph.D. thesis*.
- Mari, D., Campitelli, E., Drake, E., Krawitz, A., 2015. Finite element modeling of the WC–10 wt% co thermal stresses: build-up and phase specific strain response during cyclic loading. *Int. J. Refract. Met. Hard Mater.* 49, 256–260.
- Marshall, J.M., Giraudel, M., 2015. The role of tungsten in the co binder: effects on WC grain size and hcp–fcc co in the binder phase. *Int. J. Refract. Met. Hard Mater.* 49, 57–66.
- Mavko, G., Mukerji, T., Dvorkin, J., 1998. *The Rock Physics Handbook: Tools for Seismic Analysis in Porous Media*, 329 Pp. Cambridge Univ. Press, Cambridge, UK.
- Michel, J.-C., Suquet, P., 2016. A model-reduction approach in micromechanics of materials preserving the variational structure of constitutive relations. *J. Mech. Phys. Solids* 90, 254–285.
- Mingard, K., Gee, M., 2007. EBSD Examination of worn WC–Co hardmetal surfaces. *Wear* 263 (1), 643–652.
- Mingard, K., Roebuck, B., Marshall, J., Sweetman, G., 2011. Some aspects of the structure of cobalt and nickel binder phases in hardmetals. *Acta Mater.* 59 (6), 2277–2290.
- Morral, F., Safranek, W., 1974. Cobalt and Co alloys, 3rd edition. In: Lowenheim, F.A. (Ed.), *Modern Electroplating*. Wiley-Interscience, New York, pp. 152–164.
- Murray, M., 1977. Fracture of WC–Co alloys: an example of spatially constrained crack tip opening displacement. In: *Proceedings of the Royal Society of London A: Mathematical, Physical and Engineering Sciences*, 356. The Royal Society, pp. 483–508.
- Murray, T., Balogun, O., Steen, T., Basu, S., Sarin, V., 2005. Inspection of compositionally graded mullite coatings using laser based ultrasonics. *Int. J. Refract. Met. Hard Mater.* 23 (4), 322–329.
- Nelson, R., Milner, D., 1972. Densification processes in the tungsten carbide–cobalt system. *Powder Metall.* 15 (30), 346–363.
- Nemat-Nasser, S., Yu, N., Hori, M., 1993. Bounds and estimates of overall moduli of composites with periodic microstructure. *Mech. Mater.* 15 (3), 163–181.
- Nishimatsu, C., 1960. Experimental survey of the deformation of the hard-ductile two-phase alloy system wcco. *Trans. Am. Soc. Met.* 52, 469–484.
- Noyan, I.C., Cohen, J.B., 2013. *Residual Stress: Measurement by Diffraction and Interpretation*. Springer-Verlag.
- Okamoto, S., Nakazono, Y., Otsuka, K., Shimoitani, Y., Takada, J., 2005. Mechanical properties of WC–Co cemented carbide with larger WC grain size. *Mater. Charact.* 55 (4), 281–287.
- Olovsjö, S., Johanson, R., Falsafi, F., Bexell, U., Olsson, M., 2013. Surface failure and wear of cemented carbide rock drill buttons—the importance of sample preparation and optimized microscopy settings. *Wear* 302 (1), 1546–1554.
- Panov, V.S., Chuvilin, A.M., Falkovskiy, V.A., 2004. *Technology and Properties of Sintered Cemented Carbides (in Russian)*. Moscow, Russian Federation: MISIS.
- Pastor, H., 1999. Developments in the powder metallurgy of non-oxide cermets. In: *Advanced Science and Technology of Sintering*. Springer, pp. 461–474.
- Petch, N., 1953. The cleavage strength of polycrystals. *J. Iron Steel Inst.* 174, 25–28.
- Pickens, J., Gurland, J., 1978. The fracture toughness of WC–Co alloys measured on single-edge notched beam specimens precracked by electron discharge machining. *Mater. Sci. Eng.* 33 (1), 135–142.
- Pollock, C., Stadelmaier, H., 1970. The eta carbides in the fe–W–C and co–W–C systems. *Metallur. Trans.* 1 (4), 767–770.
- Prakash, L., 1979. Properties of tungsten carbide hard metals with fe-co-ni binder in sintered and thermally treated state. *KFK Nachrichten* (2) 35–42.
- Prakash, L., 2014. Fundamentals and general applications of hardmetals. In: Sarin, V., Mari, D., Llanes, L. (Eds.), *Comprehensive Hard Materials*. Volume I. Newnes, pp. 123–138. 1.02.
- Quey, R., Dawson, P., Barbe, F., 2011. Large-scale 3D random polycrystals for the finite element method: generation, meshing and remeshing. *Comput. Methods Appl. Mech. Eng.* 200 (17), 1729–1745.
- Ramqvist, L., 1965. Wetting of metallic carbides by liquid copper, nickel, cobalt and iron. *Int. J. Powder Metall.* 1 (4).

- Rautala, P., Norton, J.T., 1952. Tungsten-cobalt-carbon system. *Trans. AIME* 194 (4), 1045–1050.
- Reimers, W., Pyzalla, A.R., Schreyer, A., Clemens, H., 2008. *Neutrons and Synchrotron Radiation in Engineering Materials Science: From Fundamentals to Material and Component Characterization*. KGaA, Weinheim: Wiley-VCH Verlag GmbH & Co.
- Reuss, A., 1929. Berechnung der fließgrenze von mischkristallen auf grund der plastizitätsbedingung für einkristalle. *ZAMM-J. Appl. Math. Mech./Z. Angew. Math. Mech.* 9 (1), 49–58.
- Roebuck, B., Almond, E., 1988. Deformation and fracture processes and the physical metallurgy of WC–Co hard metals. *Int Mat Rev* 33, 90–110.
- Rycroft, C., 2008. *Voro++: A three-dimensional Voronoi cell library in C++*. math.lbl.gov/voro++/.
- Sadowski, T., 2005. *Modelling of Damage and Fracture Processes of Ceramic Matrix Composites*. Springer Wien NewYork.
- Sadowski, T., Nowicki, T., 2008. Numerical investigation of local mechanical properties of WC–Co composite. *Comput. Mater. Sci* 43 (1), 235–241.
- Sailer, T., Herr, M., Sockel, H.-G., Schulte, R., Feld, H., Prakash, L., 2001. Microstructure and mechanical properties of ultrafine-grained hardmetals. *Int. J. Refract. Met. Hard Mater* 19 (4), 553–559.
- Sanchez-Palencia, E., Zaoui, A., 1987. *Homogenization Techniques for Composite Media*. Lecture Notes in Physics, 272. Springer.
- Sarin, V., Johannesson, T., 1975. On the deformation of WC–Co cemented carbides. *Met. Sci.* 9 (1), 472–476.
- Schedler, W., 1988. *Hartmetalle Für Den Praktiker*. Dußelsdorf: VDI-Verlag.
- Shatov, A.V., Ponomarev, S., Firstov, S., 2014. Microstructure and morphology of hardmetals. In: Sarin, V., Mari, D., Llanes, L. (Eds.), *Comprehensive Hard Materials*. Volume I. Newnes, pp. 301–344. 1.10
- Sigl, L., Exner, H., 1987. Experimental study of the mechanics of fracture in WC–Co alloys. *Metall. Trans. A* 18 (7), 1299–1308.
- Sigl, L., Exner, H., Fischmeister, H., 1984. Characterization of fracture processes and fracture relevant parameters in WC–Co hardmetals. *Sci. Hard Mater.* 631–644.
- Slazar, M., Dusza, J., Parilak, L., 1986. Micromechanics of Fracture in WC–Co Hardmetals. In: Almond, E., Brookes, C., Warren, R. (Eds.), *Proceedings of the International Conference on Science of Hard Materials*. A Hilger Ltd, Bristol.
- Song, X., Gao, Y., Liu, X., Wei, C., Wang, H., Xu, W., 2013. Effect of interfacial characteristics on toughness of nanocrystalline cemented carbides. *Acta Mater.* 61 (6), 2154–2162.
- Spiegler, R., Fischmeister, H., 1992. Prediction of crack paths in WC–Co alloys. *Acta Metall. Mater.* 40 (7), 1653–1661.
- Struers, 2016. *Polishing method description*. www.struers.com/default.asp?print=1&doc_id=126.
- Suquet, P., 1997. *Effective Properties of Nonlinear Composites*. Springer.
- Takahashi, T., Freise, E., 1965. Determination of the slip systems in single crystals of tungsten monocarbide. *Philos. Mag.* 12 (115), 1–8.
- Tarjus, G., Schaaf, P., Talbot, J., 1991. Random sequential addition: a distribution function approach. *J. Stat. Phys.* 63 (1–2), 167–202.
- Tvergaard, V., 1990. Material failure by void growth to coalescence. *Adv. Appl. Mech.* 27 (1), 83–151.
- Voigt, W., 2014. *Lehrbuch Der Kristallphysik (Mit Ausschluss Der Kristalloptik)*. Springer-Verlag.
- Warren, R., Waldron, M., 1972. Microstructural development during the liquid-phase sintering of cemented carbides: i. wettability and grain contact. *Powder Metall.* 15 (30), 166–201.
- Weidow, J., Andrén, H.-O., 2010. Grain and phase boundary segregation in WC–Co with small v, cr or mn additions. *Acta Mater.* 58 (11), 3888–3894.
- Weidow, J., Norgren, S., Andrén, H.-O., 2009. Effect of v, cr and mn additions on the microstructure of WC–Co. *Int. J. Refract. Met. Hard Mater.* 27 (5), 817–822.
- Weisbrook, C., Krawitz, A., 1996. Thermal residual stress distribution in WC–Ni composites. *Mater. Sci. Eng.: A* 209 (1), 318–328.
- Werner, E., Siegmund, T., Weinhandl, H., Fischer, F., 1994. Properties of random polycrystalline two-phase materials. *Appl. Mech. Rev.* 47 (15), S231–S240.
- Xu, Z.-H., Ågren, J., 2004. A modified hardness model for WC–Co cemented carbides. *Mater. Sci. Eng.: A* 386 (1), 262–268.
- Z-set, 2016. *Z-set: Non-linear material and structure analysis suite*. <http://www.zset-software.com>.
- Zaoui, A., 1997. *Lecture Notes “Matériaux Hétérogènes et Composites”*. École Polytechnique.
- Zhang, H., Lu, Q., Zhang, L., Fang, Z.Z., 2010. Dependence of microcrack number density on microstructural parameters during plastic deformation of WC–Co composite. *Int. J. Refract. Met. Hard Mater.* 28 (3), 434–440.